

# A geometrical Green-Naghdi type system for dispersive-like waves in prismatic channels

Sergey Gavriluk\* and Mario Ricchiuto†

August 19, 2024

## ABSTRACT

We propose a one dimensional fully nonlinear model for surface waves in channels accounting for dispersive effects strictly related to multi-dimensional hydrostatic processes related to geometrical variations, namely to the bathymetry. Our model generalizes and improves those proposed by Chassagne et al. 2018 and 2019, as well as Quezada de Luna et al JFM 2021. The new model is obtained as an approximation of the hyperbolic shallow water equations under some hypotheses on the anisotropy of the propagation. For historical reasons the new model is referred to as geometrical Green-Naghdi type (gGN) system. The gGN system is fully nonlinear and weakly dispersive. It is endowed with an exact energy conservation law, and admits several types of exact travelling wave solutions. We analyze the propagation properties compare them to those of Chassagne et al. JFM 2019, including a characterization of undular bores via the analogy by Lemoine. Finally the system is recast in two useful forms appropriate for its numerical approximations, whose properties are discussed. Our results allow to further confirm the existence of these dispersive processes (highlighted in Chassagne et al JFM 2019) having a fully hydrostatic nature and modelled by the 2D hyperbolic nonlinear shallow water simulations. Finally, the numerical fully validate the new gGN model proposed.

## Contents

<b>1</b>	<b>Introduction</b>	<b>2</b>
<b>2</b>	<b>Equations averaged in <math>y</math>-direction</b>	<b>3</b>
2.1	Generalities and asymptotic expansion . . . . .	3
2.2	Small-scale geometrical effects on the section average flow . . . . .	5
2.3	Closed form equations . . . . .	5
2.4	Computation of the geometric parameter for the triangular and trapezoidal type bottom . . . . .	6
<b>3</b>	<b>Properties of the geometrical Green-Naghdi system</b>	<b>7</b>
3.1	Hamiltonian structure and energy equation . . . . .	7
3.2	Linear dispersion properties . . . . .	7
3.3	Travelling wave solutions: solitons . . . . .	8
3.4	Travelling waves solutions: a composite solution . . . . .	10
<b>4</b>	<b>System reformulations and numerical approximation</b>	<b>10</b>

\*Aix Marseille Univ, CNRS, IUSTI, UMR 7343, Marseille, France, [sergey.gavrilyuk@univ-amu.fr](mailto:sergey.gavrilyuk@univ-amu.fr)

†INRIA, Univ. Bordeaux, CNRS, Bordeaux INP, IMB, UMR 5251, 200 Avenue de la Vieille Tour, 33405 Talence cedex, France, [mario.ricchiuto@inria.fr](mailto:mario.ricchiuto@inria.fr)

4.1	Elliptic-Hyperbolic approximation . . . . .	11
4.2	Hyperbolic relaxation . . . . .	12
4.3	Numerical discretization . . . . .	13
4.3.1	Time stepping . . . . .	13
4.3.2	Discretization of the spatial differential operators . . . . .	14
<b>5</b>	<b>Numerical tests</b>	<b>15</b>
5.1	Verification on solitary waves . . . . .	15
5.2	Breakdown of a Gaussian water column . . . . .	15
5.2.1	Validation against section averaged 2D shallow water simulations . . . . .	17
5.3	Riemann problem . . . . .	18
5.3.1	Validation against section averaged 2D shallow water simulations . . . . .	21
5.3.2	Soliton fission . . . . .	21
5.4	Composite solution . . . . .	22
<b>6</b>	<b>Conclusion</b>	<b>24</b>

## 1 Introduction

This paper presents a new 1D non-linear dispersive model for gravity waves over topography originated by inherently hydrostatic 2D phenomena. The physical background of this work goes back to the measurements of bore propagation by [38], as well as to the in situ measurements of tidal bore propagation in the Garonne and Seine rivers, reported in [5, 6]. Before the Froude number is high enough for wave breaking to occur ( $\sim 1.3$ ), two different dispersive propagation regimes are clearly observable both in laboratory and river experiments. One of them, occurring for Froude higher than  $\sim 1.15$ , corresponds to the usual dispersive undular bore known since Favre’s experiments [15]. These waves are well understood, and can be related theoretically to the classical dispersion relation from Airy theory [27, 6]. For lower Froude numbers, longer waves are observed which do not correspond to classical dispersive propagation. This phenomenon has been studied in [11, 10] where it has been shown numerically and theoretically that these low Froude undular bore are generated by a purely geometrical process related to diffraction in the transverse direction. These waves also exist in hydrostatic flows, and, despite their dispersive nature, can be computed using the hyperbolic shallow water equations. Inspired by early work by [32, 24] on the generation of dispersive effects in linear waves propagating in anisotropic materials, in [11, 10] the idea of a horizontal/longitudinal scale separation of two propagation processes with scales  $l_y$  and  $l_x \gg l_y$  is introduced. Using the small parameter  $\varepsilon = l_y/l_x$  an asymptotic section averaged approximation of the linearized shallow water equations is derived, featuring a dispersive term with a coefficient only depending on the channel’s geometry. This dispersive process, and in particular the dispersion relation of the asymptotic PDE, allows to provide a quantitative prediction of the wavelength dependence on the Froude number for the low Froude waves. Later on [28] used the same formal development to identify solitary waves associated to geometrical dispersion. These waves are thus purely related to bathymetric effects, and in particular diffraction in the transverse direction. These multi-scale processes arising from hyperbolic models are sometimes referred to as effective dispersion [32, 24, 28, 25], and have been baptised “dispersive-like” in [11, 10].

In the present work we propose a 1D fully nonlinear model for dispersive-like waves originated from 2D bathymetric variations. In this respect, this work is inherently different from previous ones on section averaged dispersive models [39, 41]. Indeed, here we explicitly aim at describing dispersive effects only related to diffraction due to transverse bathymetric variations, and already present in purely hydrostatic and hyperbolic models such as the the Saint-Venant equations (shallow water equations). In this respect, it is less clear what processes are accounted for in previously proposed models. For example, numerical experiments in [22] seem to indicate that at least the model proposed in [41] also accounts for only such effects, despite being derived as an approximation to the full Euler equations.

The new geometrical Green-Naghdi type (gGN) model proposed in this work is derived from the nonlinear hyperbolic shallow water equations under hypotheses similar to those of [10]. We call this model Green-Naghdi type (and not, as conventionally, the Serre-Green-Naghdi type) to emphasize that it is based on the model taking into account the

effects of 2D bathymetry. Despite the fully nonlinear setting, in our derivation we keep the hypotheses of periodicity or reflective conditions at the  $y$  boundaries. So the model proposed is applicable to channels enclosed between walls with no dry banks, or periodic ones. This new gGN model is fully non-linear, it has a Hamiltonian structure, and an exact energy conservation law. We study the propagation properties of the system, and compare its dispersion relation to that of the linear model of [10], showing an agreement within the asymptotic accuracy of both models. We show several types of exact solutions including both solitary waves, and a more complex composite solution with infinite peaks. We then propose two reformulations to solve the PDE system numerically: the first based a elliptic-hyperbolic decomposition [17], the second using hyperbolic relaxation [16]. We discuss the numerical approximation of both formulations, and provide a thorough numerical study. We numerically show that the model approximates accurately section averaged numerical computations performed with a 2D shallow water code on several examples.

The structure of the paper is the following. In section §2 we introduce the asymptotic hypothesis and discuss the forma derivation of the model. Section §3 is devoted to the study of some of its properties: energy conservation law, dispersion relation, travelling wave solutions. In section §4 we propose some re-formulations of the system more suitable for its numerical approximation, and discuss the numerical methods implemented to this end. In section §5 we provide numerical studies of to verify the implementation, to compare the different formulations proposed, study the behaviour of the new model, and validate it using averaged 2D shallow water computations. Comparisons are made with the standard Serre-Green-Naghdi model when possible. The paper is ended by some considerations on future developments, and extension.

## 2 Equations averaged in $y$ -direction

We consider shallow water flows over topography described by the classical 2D Saint-Venant equations :

$$h_t + (hu)_x + (hv)_y = 0, \quad (1a)$$

$$(hu)_t + (hu^2 + gh^2/2)_x + (huv)_y = -ghb_x, \quad (1b)$$

$$(hv)_t + (huv)_x + (hu^2 + gh^2/2)_y = -ghb_y. \quad (1c)$$

Here  $t$  is time,  $(x, y)$  are the Cartesian coordinates,  $(u, v)$  are the corresponding fluid velocities,  $z = b(x, y)$  is the bottom topography, and  $g$  is the acceleration of gravity. Introducing dimensionless variables with the ‘tilde’ sign

$$x = L\tilde{x}, \quad y = \varepsilon L\tilde{y}, \quad t = L/\sqrt{gH}\tilde{t}, \quad u = \sqrt{gH}\tilde{u}, \quad v = \varepsilon\sqrt{gH}\tilde{v},$$

$$h = H\tilde{h}, \quad b = H\tilde{b},$$

and suppressing in the following the sign ‘tilde’, one obtains then the following dimensionless equations

$$h_t + (hu)_x + (hv)_y = 0, \quad (2a)$$

$$u_t + uu_x + vu_y + (h + b)_x = 0, \quad (2b)$$

$$\varepsilon^2(v_t + uv_x + vv_y) + (h + b)_y = 0, \quad (2c)$$

with a small parameter  $\varepsilon$  characterising the ratio of the characteristic scales in  $y$  and  $x$  directions. We consider only the case  $b = b(y)$  and suppose that either  $b(y)$  is  $l$ - periodic function ( $b(y) = b(l + y)$ ), or that slip wall/reflective conditions hold for  $y = 0$  and  $y = l$ . Our aim is to propose equivalent 1D equations, which we will show exhibit a dispersive behaviour, similarly to what already proved in [10]. Figure 1 shows typical channel geometries encountered in practice, and gives some initial geometrical notation.

### 2.1 Generalities and asymptotic expansion

We will use the two types of averaging operators in  $y$ -direction One is standard :

$$\bar{f}(t, x) = \frac{1}{l} \int_0^l f(t, x, y) dy \quad (3)$$

for any  $l$ -periodic in  $y$ -direction function  $f(t, x, y)$ . The second one defines the weight averaged value

$$\langle f \rangle = \frac{1}{lh} \int_0^l h(t, x, y) f(t, x, y) dy. \quad (4)$$



Figure 1: Typical channel sections of period  $l$  with  $l = l_1 + l_2$  for the triangular periodic bottom ( $b(0) = b(l)$ ,  $b(l_1) = 0$ ), and for the trapezoidal bottom ( $b(0) = b(l)$ ,  $l = l_1 + l_2 + l_3$ ,  $b(y) = 0$ ,  $l_1 \leq y \leq l_1 + l_2$ ).

Sometimes the last averaging is called *Favre averaging*. The advantage of the last definition is that the mass conservation law is exactly satisfied in a usual sense, with the velocity  $\langle u \rangle$ . The dimensionless averaged conservative form of equations (1a), (1b) in the case  $b = b(y)$  becomes :

$$\bar{h}_t + (\bar{h}\langle u \rangle)_x = 0, \quad (5a)$$

$$(\bar{h}\langle u \rangle)_t + (\overline{hu^2} + \frac{1}{2}\overline{h^2})_x = 0, \quad (5b)$$

We need no to find  $\overline{hu^2}$  and  $\overline{h^2}$ . Equation (2c) implies :

$$h + b = \bar{h} + \bar{b} + \mathcal{O}(\varepsilon^2). \quad (6)$$

We want to find this  $\mathcal{O}(\varepsilon^2)$  term in (6) in explicit form. For this, let us suppose the following ansatz for the velocity field :

$$u(t, x, y) = \langle u \rangle(t, x) + \varepsilon^2 u_1(t, x, y) + \mathcal{O}(\varepsilon^3), \quad v = v_0(t, x, y) + \mathcal{O}(\varepsilon), \quad (7)$$

having the properties

$$\overline{hu_1} = 0. \quad (8)$$

In particular, it implies that

$$\overline{hu^2} = \bar{h}\langle u \rangle^2 + \mathcal{O}(\varepsilon^3) \quad (9)$$

This ansatz means that the shear effects in  $y$ -direction are negligible, i.e. the velocity in  $x$ -direction is almost  $y$ -independent (see [30] for the derivation of the model with shear effects, but without dispersive effects). An additional hypothesis about the behavior of  $v_0$  will be now specified. Replacing ansatz (7) into the mass conservation law (2a), one obtains for  $v_0$  the equation :

$$\bar{h}_t + (\langle u \rangle(\bar{h} + \bar{b} - b))_x + (v_0(\bar{h} + \bar{b} - b))_y = \mathcal{O}(\varepsilon). \quad (10)$$

Since

$$\bar{h}_t + (\bar{h}\langle u \rangle)_x = 0,$$

one gets

$$(\langle u \rangle(\bar{b} - b))_x + (v_0(\bar{h} + \bar{b} - b))_y = \mathcal{O}(\varepsilon).$$

It implies the following expression in the zero order approximation with respect to  $\varepsilon$  :

$$v_0(\bar{h} + \bar{b} - b) \approx C(t, x) - S(y) \langle u \rangle_x, \quad S(y) = \int_0^y (\bar{b} - b(y')) dy'.$$

Here  $C(t, x)$  is a function of only  $t$  and  $x$  which should be defined from an additional condition. The function  $S(y)$  has the property:  $S(0) = S(l) = 0$ . For the applications we have in mind, we can use as conditions the requirement of a vanishing average discharge in the  $y$ -direction :

$$\int_0^l v_0 h dy = \int_0^l v_0 (\bar{h} + \bar{b} - b) dy = 0,$$

i. e.  $C(t, x) = \bar{S} \langle u \rangle_x$ .

## 2.2 Small-scale geometrical effects on the section average flow

Using the condition on the transverse average velocity we can now write

$$v_0(\bar{h} + \bar{b} - b) \approx (\bar{S} - S(y)) \langle u \rangle_x. \quad (11)$$

In particular, (11) gives us

$$v_0(t, x, y) \approx \frac{(\bar{S} - S(y))}{\bar{h} + S_y} \langle u \rangle_x = -\frac{D\bar{h}}{Dt} \frac{(\bar{S} - S(y))}{\bar{h}^2} \sum_{n=0}^{\infty} (-1)^n \frac{S_y^n}{\bar{h}}, \quad (12)$$

with the operator of total derivative along the one-dimensional velocity field  $\langle u \rangle$  :

$$\frac{D}{Dt} = \frac{\partial}{\partial t} + \langle u \rangle \frac{\partial}{\partial x}. \quad (13)$$

Thus, we are able to find  $\mathcal{O}(\varepsilon^2)$  terms from (2c):

$$(h + b)_y \approx -\varepsilon^2(v_t + uv_x + vv_y) \approx -\varepsilon^2 \left( \frac{Dv_0}{Dt} + v_0(v_0)_y \right). \quad (14)$$

If one takes only the term of zero order in  $n$  in (12), one obtains

$$v_0(t, x, y) \approx -\frac{\bar{S} - S(y)}{\bar{h}^2} \frac{D\bar{h}}{Dt} = (\bar{S} - S(y)) \dot{\tau}, \quad \dot{\tau} = \frac{D\tau}{Dt}, \quad \tau = \frac{1}{\bar{h}}. \quad (15)$$

Setting

$$\sigma = \bar{S} - S(y), \quad D = \int_0^y \sigma(y') dy', \quad (16)$$

and using (15) one obtains up to  $\varepsilon$  terms

$$v_t \approx \sigma \partial_t \dot{\tau} \quad (17)$$

$$uv_x \approx \sigma \langle u \rangle \partial_x \dot{\tau} \quad (18)$$

$$vv_y = (v^2/2)_y \approx (\sigma^2 \dot{\tau}^2/2)_y = (\sigma^2/2)_y \dot{\tau}^2 \quad (19)$$

so

$$(h + b)_y \approx -\varepsilon^2 \{ \sigma \ddot{\tau} + (\sigma^2/2)_y \dot{\tau}^2 \} \quad (20)$$

Finally,

$$h + b \approx \bar{h} + \bar{b} - \varepsilon^2 \left( (D - \bar{D}) \ddot{\tau} + \frac{1}{2} \dot{\tau}^2 (\sigma^2 - \bar{\sigma}^2) \right), \quad (21)$$

## 2.3 Closed form equations

We can now evaluate

$$\begin{aligned} \bar{h}^2 &= \overline{\left\{ \bar{h} + \sigma_b(y) - \varepsilon^2 \left( (D - \bar{D}) \ddot{\tau} + \frac{1}{2} \dot{\tau}^2 (\sigma^2 - \bar{\sigma}^2) \right) \right\}^2} \\ &= \bar{h}^2 + \bar{\sigma}_b^2 + \varepsilon^4 \overline{\left( (D - \bar{D}) \ddot{\tau} + \frac{1}{2} \dot{\tau}^2 (\sigma^2 - \bar{\sigma}^2) \right)^2} \\ &\quad + 2\bar{h}\bar{\sigma}_b - 2\varepsilon^2 \bar{h} \overline{\left( (D - \bar{D}) \ddot{\tau} + \frac{1}{2} \dot{\tau}^2 (\sigma^2 - \bar{\sigma}^2) \right)} - 2\varepsilon^2 \bar{\sigma}_b \overline{\left( (D - \bar{D}) \ddot{\tau} + \frac{1}{2} \dot{\tau}^2 (\sigma^2 - \bar{\sigma}^2) \right)} \end{aligned}$$

having set  $\sigma_b := \bar{b} - b(y)$ . Using all the previous definitions the first two terms on the last line are identically zero, and we obtain that

$$\begin{aligned} \bar{h}^2 &= \bar{h}^2 - 2\varepsilon^2 \bar{\sigma}_b \overline{\left( (D - \bar{D}) \ddot{\tau} + \frac{1}{2} \dot{\tau}^2 (\sigma^2 - \bar{\sigma}^2) \right)} \\ &\quad + \varepsilon^4 \overline{\left( (D - \bar{D}) \ddot{\tau} + \frac{1}{2} \dot{\tau}^2 (\sigma^2 - \bar{\sigma}^2) \right)^2} + \bar{\sigma}_b^2 \end{aligned} \quad (22)$$

Denoting now by

$$\chi_1 := \overline{\sigma_b D}, \quad \chi_2 := \frac{1}{2} \overline{\sigma_b \sigma^2} \quad (23)$$

we can write (by neglecting the terms of order  $\varepsilon^4$ ):

$$\frac{\overline{h^2}}{2} \approx \frac{\overline{h}^2}{2} + \frac{\overline{\sigma_b^2}}{2} - \varepsilon^2 (\chi_1 \ddot{\tau} + \chi_2 \dot{\tau}^2) \quad (24)$$

Let us remark that  $\chi_2 = 0$ . Indeed,

$$2\chi_2 = \overline{\sigma_b \sigma^2} = \overline{\frac{dS}{dy} (\overline{S^2} - 2\overline{S}S + S^2)} \quad (25)$$

$$= \overline{\frac{dS}{dy} \overline{S^2} - 2\overline{S} \frac{dS}{dy} S + \frac{dS}{dy} S^2} \quad (26)$$

$$= \overline{S^2 \frac{dS}{dy} - S \frac{dS^2}{dy} + \frac{dS^3}{dy}} = 0, \quad (27)$$

since  $S(0) = S(l) = 0$ . Hence,

$$\frac{\overline{h^2}}{2} = \frac{\overline{h}^2}{2} + \frac{\overline{\sigma_b^2}}{2} - \varepsilon^2 \chi_1 \ddot{\tau} \quad (28)$$

Let us prove that  $\chi_1$  is positive. Indeed,

$$\begin{aligned} \chi_1 = \overline{\sigma_b D} &= \overline{\frac{dS}{dy} \int_0^y (\overline{S} - S(y')) dy'} = \overline{S y \frac{dS}{dy} - \frac{dS}{dy} \int_0^y S(y') dy'} \\ &= \overline{S \left( \frac{d(Sy)}{dy} - S \right) - \left( \frac{d}{dy} \left( S \int_0^y S(y') dy' \right) - S^2 \right)} = \overline{S^2} - \overline{S^2} > 0. \end{aligned} \quad (29)$$

The geometric parameter  $\chi_1$  has thus a very simple meaning: it is the variance over the period of the function  $S(y) = \int_0^y (\overline{b} - b(y')) dy'$ . Since  $\overline{\sigma_b^2} = \text{const}$  (we assumed that  $b$  does not depend on  $x$ ), the system (5a) - (5b) derived up to  $\varepsilon^2$  terms becomes :

$$\overline{h}_t + (\overline{h}\langle u \rangle)_x = 0, \quad (30)$$

$$(\overline{h}\langle u \rangle)_t + (\overline{h}\langle u \rangle^2 + \frac{\overline{h^2}}{2} + p)_x = 0, \quad (31)$$

where we set

$$p = -\varepsilon^2 \chi \dot{\tau}, \quad \tau = \frac{1}{\overline{h}} \quad (32)$$

with  $\chi$  given by (29), having dropped the subscript  $_1$  for simplicity.

## 2.4 Computation of the geometric parameter for the triangular and trapezoidal type bottom

The value of the parameter  $\chi$  for a triangular type bottom (see Figure 1) is :

$$\chi = \frac{b_0^2 (l_1^2 + 4l_1 l_2 + l_2^2)}{720}.$$

Here  $b_0$  is the bottom height ( $b_0 = b(0) = b(l)$ ), and  $l_1$  is the position of the bottom singularity ( $b(l_1) = 0$ , and  $l = l_1 + l_2$ ). The value of the parameter  $\chi$  for a trapezoidal type bottom is :

$$\chi = \frac{b_0^2 (l_1 + l_3) (l_1^3 + l_1^2 (6l_2 + 5l_3) + l_3 (15l_2^2 + 6l_2 l_3 + l_3^2)) + l_1 (15l_2^2 + 24l_2 l_3 + 5l_3^2)}{720 (l_1 + l_2 + l_3)^2}.$$

Here  $b_0$  is the bottom height ( $b_0 = b(0) = b(l)$ ),  $l_1$  is the position of the first bottom singularity ( $b(l_1) = 0$ ),  $l_1 + l_2$  is the position of the second bottom singularity ( $b(l_1 + l_2) = 0$ ),  $b(y) = 0$  for  $y \in (l_1, l_1 + l_2)$ , and  $l = l_1 + l_2 + l_3$ .

The formulas coincide if one takes  $l_2 = 0$  and replaces  $l_3$  by  $l_2$ . Moreover the two formulas are symmetric with respect the pairs  $(l_1, l_2)$  and  $(l_1, l_3)$ , respectively. This implies that the dispersion effects are insensitive to mirroring of

asymmetric shapes, as one should expect. Similarly, one easily verifies that asymmetric configurations have a smaller dispersion coefficient than symmetric ones. For this, one has to look for the minimum of  $\chi$  under the constraint  $l_1 + l_2 = l$  in the case of the triangular type bottom, or under the constraint  $l_1 + l_2 + l_3 = l$  in the case of trapezoidal type bottom. For the triangular bottom topography, the maximal value of  $\chi/(b_0^2 l^2)$  is achieved for  $l_1 = l_2 = l/2$ , and is equal approximately to 0.0020833. For the trapezoidal bottom the maximal value of  $\chi/b_0^2 l^2$  is achieved for  $l_1 = l_3 = (21 - \sqrt{41})l/40$ , and is equal approximately to 0.0027139.

### 3 Properties of the geometrical Green-Naghdi system

#### 3.1 Hamiltonian structure and energy equation

Using standard techniques [18, 36], we can show that system (30)-(31) are the Euler-Lagrange equations for the Hamilton action

$$a = \int_{t_0}^{t_1} L dt,$$

under the constraint (30) which is the mass conservation. Here  $t_i, i = 0, 1$ , are given time instants, and the Lagrangian  $L$  is defined by :

$$L = \int_{-\infty}^{+\infty} \left( \bar{h} \frac{\langle u \rangle^2}{2} - W(\tau, \dot{\tau}) \right) dx, \quad (33)$$

with

$$W(\tau, \dot{\tau}) = \frac{g\bar{h}^2}{2} - \frac{\chi \bar{h} \dot{\tau}^2}{2}, \quad \tau = \frac{1}{\bar{h}}.$$

The system admits the energy conservation law

$$\left( \bar{h} \left( \frac{\langle u \rangle^2}{2} + \frac{\bar{h}}{2} + \frac{\varepsilon^2 \chi \dot{\tau}^2}{2} \right) \right)_t + \left( \bar{h} \langle u \rangle \left( \frac{\langle u \rangle^2}{2} + \frac{\bar{h}}{2} + \frac{\varepsilon^2 \chi \dot{\tau}^2}{2} \right) + \left( \frac{\bar{h}^2}{2} + p \right) \langle u \rangle \right)_x = 0. \quad (34)$$

which is a consequence of invariance of the Lagrangian under time shift.

#### 3.2 Linear dispersion properties

Consider now the linearized version of (30), (31) and (32) in dimensional form:

$$\bar{h}_t + \bar{h}_0 \langle u \rangle_x = 0, \quad (35)$$

$$\langle u \rangle_t + g \bar{h}_x = \frac{\chi}{\bar{h}_0} \langle u \rangle_{xxt}, \quad (36)$$

with  $\chi$  having the dimension  $[m^4]$  in dimensional form. Using standard techniques we show that the dispersion relation of the system is

$$\omega^2 = k^2 \frac{g \bar{h}_0}{1 + \frac{\chi}{\bar{h}_0^2} k^2} \quad (37)$$

with  $k$  the wavenumber. A similar result can be obtained by combining (35) and (36) to obtain the wave equation

$$\bar{h}_{tt} - \frac{\chi}{\bar{h}_0} \bar{h}_{xxtt} - g \bar{h}_0 \bar{h}_{xx} = 0 \quad (38)$$

which naturally also leads to the dispersion relation (37). The latter expressions can be compared to the asymptotic wave equation derived in [10] which reads

$$\zeta_{tt} - g \bar{h}_0 \zeta_{xx} - g \bar{h}_0 \chi^* \zeta_{xxxx} = 0 \quad (39)$$

with a dispersion relation

$$\omega^2 = k^2 g \bar{h}_0 (1 - \chi k^2) \quad (40)$$

where, as in our case,  $\chi^*$  is a dispersion coefficient related to geometrical/bathymetric effects. Note that although the asymptotic approximations (39) and (38) are equivalent within an asymptotic rest of order  $\varepsilon^4$ , the geometrical dispersion coefficients are obtained in a slightly different way. In the pictures of the second column in figure 2 we compare the two models for three different sections: a triangular one with  $b_0/l_1 = 1/6$  (first row), a trapezoidal one

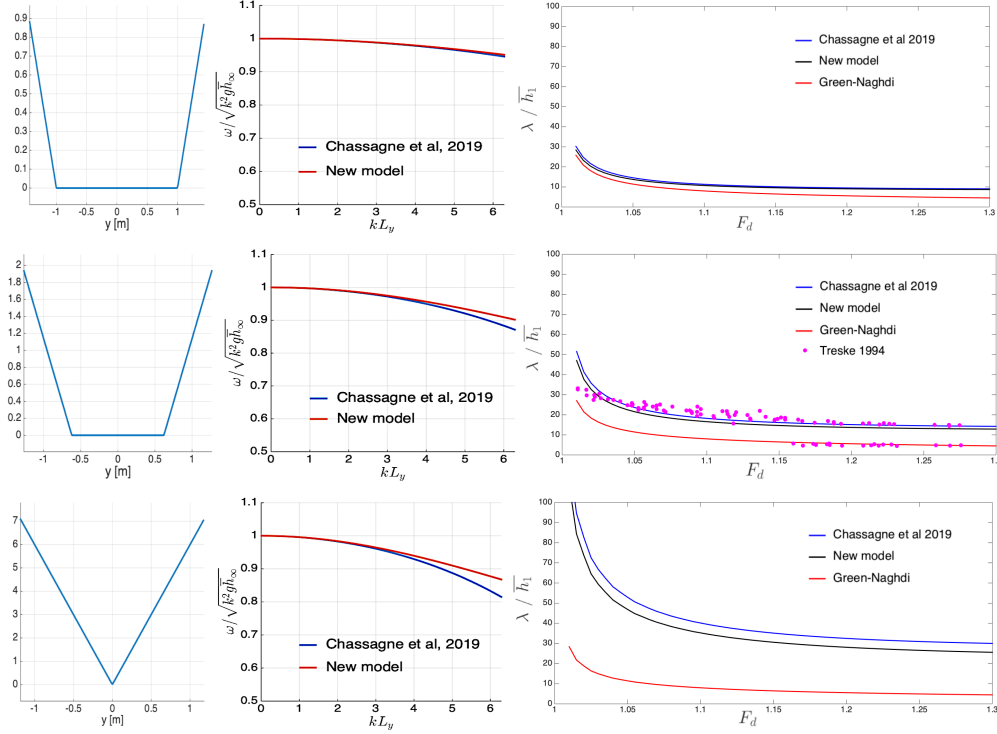


Figure 2: Dispersion relation: comparison with the model of [10] for three different sections.

with  $b_0/l_1 = 1/3$  (second row), and a steeper trapezium with  $b_0/l_1 = 1/2$  (last row). For completeness the section shapes are reported in the first column. The dispersion relation curves (middle column) show that the new model and the one proposed in [10] have almost identical dispersive behaviour for reduced wave-numbers up to  $kl = \pi$ . We can observe differences for shorter waves, which are however within classical modelling error. Finally, following we use the dispersion relation to predict the wavelength-Froude number relation for the sections considered, using the physical analogy by Lemoine (please refer to [10, 27] for details). The results are reported in the rightmost pictures of the figure 2, including a comparison with the predictions obtained using the model by [10], as well as with the curves obtained using the classical Serre-Green-Naghdi model. The new gGN model provides a satisfactory prediction of the wavelengths of the dispersive like waves measured in [38, 6] (rightmost picture, second row). These results show that the main propagation features of these waves are well represented by the new gGN system. For completeness, we also report experimental data for the shorter waves measured in [38, 6]. These are essentially classical Favre waves and agree very well with the Serre-Green-Naghdi curve, consistently with the numerical results by [10].

### 3.3 Travelling wave solutions: solitons

We show in this section that the system derived admits exact travelling wave solutions. We focus here on solitary waves. We consider solitons of amplitude  $a$  and celerity  $c$  travelling on a far field with constant averaged depth  $\bar{h}_\infty$ . So, let us set  $\xi = x - ct$  and assume that at time  $t = 0$  the peak is at  $x = 0$ . We now seek solutions of the form

$$\bar{h} = \bar{h}(\xi), \quad \langle u \rangle = \langle u \rangle(\xi)$$

We can readily write from the mass conservation law that

$$\bar{h}(\langle u \rangle - c) = m = \text{const},$$

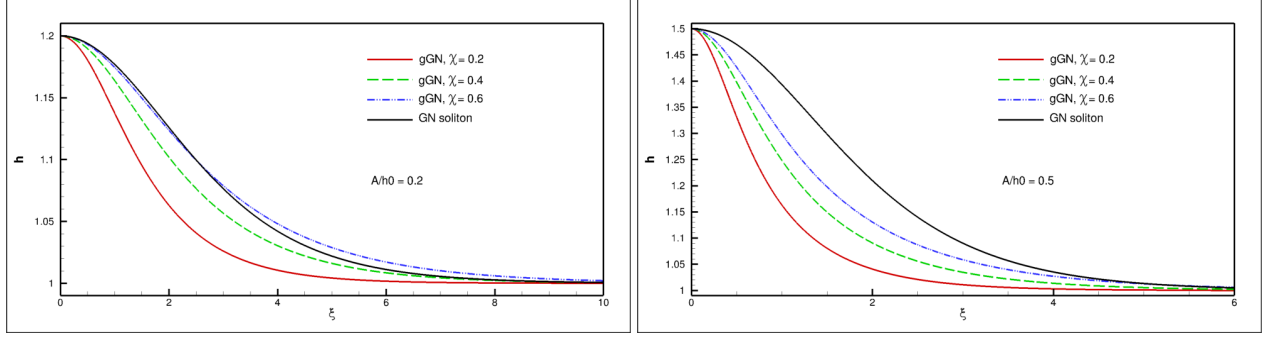
Which using the conditions at infinity gives the relations

$$\langle u \rangle = \left(1 - \frac{\bar{h}_\infty}{\bar{h}}\right)c, \quad m = -\bar{h}_\infty c \quad (41)$$

The momentum equation implies :

$$\bar{h}(\langle u \rangle - c)^2 + \frac{g\bar{h}^2}{2} - \chi\bar{\tau} = q = \text{const}. \quad (42)$$




 Figure 3: Solitary waves obtained for different values of  $\chi$ , and for  $\epsilon = 0.2$  (left) and  $\epsilon = 0.5$  (right).

Since  $\ddot{\tau} = (\langle u \rangle - c)((\langle u \rangle - c)\tau')' = m^2\tau(\tau\tau')'$  (here 'prime' means the derivative with respect to  $\xi$ ), one obtains :

$$m^2\tau + \frac{g}{2\tau^2} - \chi m^2\tau(\tau\tau')' = q = \text{const.} \quad (43)$$

Let  $\tau_\infty = 1/\bar{h}_\infty$ . Then one can find  $q$  and we have :

$$m^2(\tau - \tau_\infty) + \frac{g}{2} \left( \frac{1}{\tau^2} - \frac{1}{\tau_\infty^2} \right) - \chi m^2\tau(\tau\tau')' = 0. \quad (44)$$

Multiplying by  $\tau'$ , one can integrate it again :

$$m^2(\tau - \tau_\infty)^2 + g \left( -\frac{1}{\tau} + \frac{1}{\tau_\infty} - \frac{\tau}{\tau_\infty^2} + \frac{1}{\tau_\infty} \right) - \chi m^2(\tau\tau')^2 = 0.$$

We rewrite this equation as

$$\chi m^2\tau^2\tau'^2 = F(\tau), \quad F(\tau) = m^2(\tau - \tau_\infty)^2 - \frac{g}{\tau\tau_\infty^2}(\tau - \tau_\infty)^2. \quad (45)$$

One can remark that at  $\tau = \tau_\infty$ , one has  $F = 0$ ,  $F' = 0$ . Moreover,  $F'' > 0$  if  $m^2 > g/\tau_\infty^3$ . If the velocity  $\langle u \rangle_\infty = 0$ , the last inequality means that the Froude number should be large than one (a classical inequality for the existence of solitary waves). Since  $F \rightarrow -\infty$  as  $\tau \rightarrow 0$ , it implies that there exists  $\tau_0 < \tau_\infty$  such that  $F(\tau_0) = 0$ . It implies the existence of supersonic solitary waves having the amplitude  $a = \bar{h}_0 - \bar{h}_\infty$ ,  $\bar{h}_0 = 1/\tau_0$ .

We can now evaluate the above relation at the peak, where  $\tau' = 0$  we have  $\tau_0 = 1/\bar{h}_0 = 1/(\bar{h}_\infty + a)$ . We thus obtain a relation celerity/amplitude:

$$0 = m^2 \frac{a^2}{\bar{h}_\infty^2(\bar{h}_\infty + a)^2} - \frac{ga^2}{\bar{h}_\infty + a}$$

Using the constancy of  $m$  we can also deduce  $m^2 = c^2\bar{h}_\infty^2$  which allows to derive the compatibility relations

$$c^2 = g(\bar{h}_\infty + a) = g\bar{h}_0 = \frac{g}{\tau_0}, \quad m^2 = g(\bar{h}_\infty + a)\bar{h}_\infty^2 = \frac{g}{\tau_0\tau_\infty^2} \quad (46)$$

Combining all of the above results we end with the nonlinear ODE

$$\tau'^2 = \frac{(\tau - \tau_\infty)^2(\tau - \tau_0)}{\chi\tau^3}. \quad (47)$$

The simplest way to solve it is to construct only a half-width solitary wave with initial condition  $\tau = \tau_0$  at  $\xi = 0$ .

In practice, we have actually solved (44) using the basic `odeint` method in `numpy`, starting from the peak with given zero derivative, and the known value of  $\tau = \tau_0$ . Typical shapes of the solitons obtained for two different values of the non-linearity  $\epsilon = a\tau_\infty$ , and of the dispersion parameter  $\chi$  are reported in figure 3. For sake of comparison, the SGN soliton with the same amplitude has been reported. Clearly, the solitons of the new system have a different shape, and a strong dependence of the latter on the relative values of  $\chi$  and  $\epsilon$ .

### 3.4 Travelling waves solutions: a composite solution

Obviously, equation (43) also solutions of other forms than solitary waves, including e.g. periodic solutions. We use this here to construct a more general family of waves including a discontinuity in between. To this end we follow the approach by [19] to compute singular (discontinuous) solutions to our system. The generic periodic solution is given by equation (43) which can be written in the form

$$\chi\tau^3(\tau')^2 = (\tau - \tau_1)(\tau - \tau_2)(\tau - \tau_3), \quad 0 < \tau_1 < \tau_2 < \tau_3, \quad m^2\tau_1\tau_2\tau_3 = g. \quad (48)$$

If  $\tau_2 = \tau_3 = \tau_\infty$ , one obtains the equation (47). The solution thus oscillates between  $\tau_1$  and  $\tau_2$ . To construct a singular stable solution, we proceed as follows (see [19] for more details)

1. Choose the roots  $0 < \tau_1 < \tau_2 < \tau_3$ , with the roots  $\tau_2$  and  $\tau_3$  close to each other;
2. Choose arbitrary the value of velocity corresponding to the state  $\tau_2$ . For example,  $u_2 = 0$ . Then, we know  $m$ . Choose  $m < 0$  (right facing periodic wave). Compute the the velocity  $D$  of the periodic traveling wave from  $h_2(u_2 - D) = m$ ,  $h_2 = 1/\tau_2$ . Thus, the periodic traveling wave is perfectly defined;
3. From equation (48) we know the value of the second derivative  $\tau''|_{\tau=\tau_1}$  :

$$2\chi\tau_1^3\tau'' = (\tau_1 - \tau_2)(\tau_1 - \tau_3) > 0. \quad (49)$$

4. Let us compute a constant state with index  $\star$  defined from the Rankine -Hugoniot relations for mass and momentum :

$$m = (u_\star - D)/\tau_\star, \quad (50)$$

$$m^2\tau_1 + \frac{g}{2\tau_1^2} - \chi m^2\tau_1^2\tau''|_{\tau=\tau_1} = m^2\tau_\star + \frac{g}{2\tau_\star^2}. \quad (51)$$

Take the root  $\tau_\star$  close to  $\tau_2$ .

5. Then the solution having the constant state  $\star$  on the left and the corresponding periodic traveling wave on the right, is stable : it contains a jump at which the generalized Rankine-Hugoniot conditions are satisfied.
6. Introduce a regularization of the jump using e.g. a half solitary wave from  $h_\star = 1/\tau_\star$  to  $h_1 = 1/\tau_1$  (in  $h$  variables ).

To build the above solution in practice we need to solve for  $\tau_\star$  given the three roots, and integrate the ODE (48) starting from  $\tau_1$  to compute the periodic branch. As for the solitary wave, this is done in practice not using the first order ODE which introduces the issue of choosing the sign of  $\tau'$  when taking the square root. We have instead recast (48) as

$$2\chi(\tau\tau')' = \left(1 - \frac{\tau_2}{\tau}\right)\left(1 - \frac{\tau_3}{\tau}\right) + \left(1 - \frac{\tau_1}{\tau}\right)\left(1 - \frac{\tau_3}{\tau}\right) + \left(1 - \frac{\tau_1}{\tau}\right)\left(1 - \frac{\tau_2}{\tau}\right) - \left(1 - \frac{\tau_1}{\tau}\right)\left(1 - \frac{\tau_2}{\tau}\right)\left(1 - \frac{\tau_3}{\tau}\right) \quad (52)$$

and integrated the above with initial conditions  $(\tau, \tau') = (\tau_1, 0)$  using the 8th order Runge-Kutta method in the SciPy class `solve_ivp`, with relative and absolute tolerances `rtol=10-8` and `atol=10-12`. Concerning the regularization, we have computed the half soliton as discussed in the previous section.

To show an example, taking  $\tau_1 = 1\text{m}^{-1}$ ,  $\tau_2 = 1.3\text{m}^{-1}$ , and  $\tau_3 = 1.301\text{m}^{-1}$ , and setting  $\chi = 0.4\text{m}^4$ , we obtain  $\tau_\star = 1.30050031985595\text{m}^{-1}$ . Integrating the ODEs we obtain the solution plotted on figure 4. Three treatments of the jump are compared: the one obtained using a gGN soliton, a Gaussian  $e^{-(x/L)^2}$  with  $L = 8\text{m}$ , and no regularization. We will compare the evolution of the three later in the results section.

## 4 System reformulations and numerical approximation

We consider in this section different re-formulations of the PDE system in view of its numerical discretization. We propose two variants. The first is based on a splitting of the original system in its elliptic and hyperbolic parts. This is a rather classical way to solve the equations, used in many works over the years [40, 26, 7, 31, 21]. More specifically, here we follow the reformulation proposed in [17, 23] for the Serre-Green-Naghdi equations, and in [9, 37, 22] for other types of Boussinesq models.

The second approach is based on a hyperbolization of the dispersive system which follows the early works by [29, 16, 8]. In particular, since the homogenized equations (30), (31), (32) admit a variational formulation (33), the hyperbolic approximation of the homogenized model is derived by using the method of augmented Lagrangian proposed in [16, 12]. This method has been justified for the Serre-Green-Naghdi equations (the case of flat bottom) in [13]. Compared to classical relaxation methods, the method of augmented Lagrangian conserves the variational structure

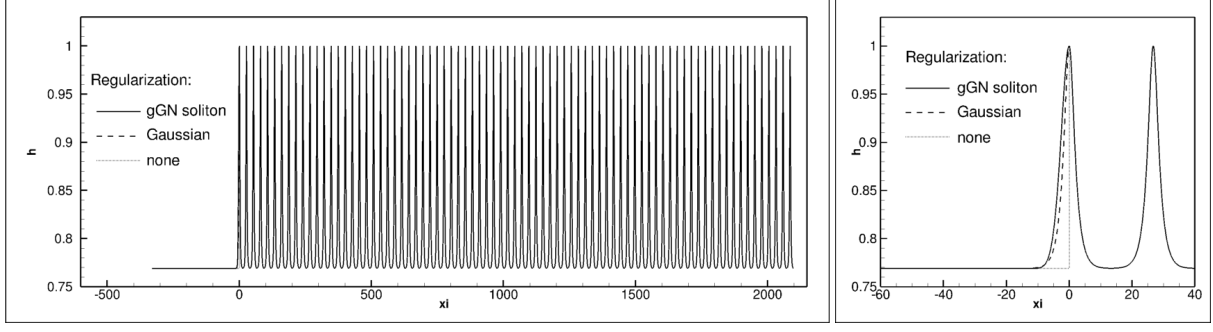


Figure 4: Composite solution obtained for  $\tau_1 = 1\text{m}^{-1}$ ,  $\tau_2 = 1.3\text{m}^{-1}$ , and  $\tau_3 = 1.301\text{m}^{-1}$ , and  $\chi = 0.4\text{m}^4$ . Left: entire solution computed on the domain  $[-350, 2100]$ m. Right: zoom of the regularized jump and first peak

of the governing equations. In particular, as in the case of homogenized equations (30), (31), (32), the hyperbolic governing equations will imply the energy conservation law as a direct consequence of the Noether theorem.

To simplify the notation, in this section we will drop the  $\bar{\cdot}$  and  $\langle \cdot \rangle$  notations for the averaged depth and Favre averaged velocity, and simply refer to these quantities as  $h$  and  $u$ . Also, we remove the  $\varepsilon$  coefficient by going back to dimensional quantities. In particular,  $\chi$  will have dimensions  $[\chi] = [b_0^2 \times \ell^2] = \text{m}^4$ .

#### 4.1 Elliptic-Hyperbolic approximation

We consider a first rewriting of the system as a perturbation to the shallow water equations via an algebraic source. The compatibility with the original equations leads to an elliptic problem for the latter. To obtain this form, we start by using the relation

$$h^2 \ddot{\tau} = h(u_x)^2 + h(u_{xt} + uu_{xx}) = h(u_x)^2 + h\dot{u}_x = h(u_t + uu_x)_x = h(\dot{u})_x \quad (53)$$

where evidently

$$\dot{u}_x = (u_{xt} + uu_{xx}) \neq (\dot{u})_x = (u_t + uu_x)_x.$$

Using the above, equation (31) can be recast as

$$(hu)_t + (hu^2 + g\frac{h^2}{2})_x = [\frac{\chi}{h}(\dot{u})_x]_x \quad (54)$$

Now following [17] we set

$$h\phi := (hu)_t + (hu^2 + gh^2/2)_x \Rightarrow \phi - gh_x = \dot{u} \quad (55)$$

We can now combine the above definition with the compatibility requirement

$$h\phi = [\frac{\chi}{h}(\dot{u})_x]_x$$

and obtain the equation for  $\phi$ :

$$h\phi = [\frac{\chi}{h}(\phi - gh_x)]_x.$$

The dispersive system (30), (31), (32) can thus be recast as

$$\begin{aligned} h\phi - \chi[\frac{1}{h}(\phi - gh_x)]_x &= 0 \\ h_t + (hu)_x &= 0 \\ (hu)_t + (hu^2 + gh^2/2)_x &= h\phi \end{aligned} \quad (56)$$

which gives two operators. The first an elliptic problem for the auxiliary variable  $\phi$  with variational form reading

$$\int v h\phi + \chi \int v_x \tau \phi_x = \chi \int v_x \tau \delta_x \quad (57)$$

where  $v$  is a test function with compact support  $v \in H_0^1$ , and having set  $\delta = gh_x$ . We can have the following simple characterization.

**Proposition 1.** *Elliptic-hyperbolic approximation: elliptic coercivity. Provided there exist solution independent uniformly bounded values  $h_{\min}$ , and  $h_{\max}$  such that  $h \in (h_{\min}, h_{\max})$ , then the variational form (57) is uniformly (wrt the solution) coercive.*

*Proof.* Under the hypotheses made, we can easily show the  $H^1$  norm equivalence

$$\frac{\chi C_{\min}}{h_{\max}} \|\phi\|_{H^1}^2 \leq \int h\phi^2 + \chi \int \tau(\phi_x)^2 \leq \frac{\chi C_{\max}}{h_{\min}} \|\phi\|_{H^1}^2$$

for any  $C_{\max} \geq \max(1, \frac{h_{\min} h_{\max}}{\chi})$  and  $C_{\max} \leq \min(1, \frac{h_{\min} h_{\max}}{\chi})$ . □

The remaining two equations provide an hyperbolic evolution operator for the shallow water variables, with an extra algebraic forcing term linear in  $\phi$ . This system can be effectively integrated in time and space.

## 4.2 Hyperbolic relaxation

We introduce the second order evolution equation for a new variable  $\eta(t, x)$  which approximates the variable  $\tau(t, x) = 1/h(t, x)$ , and write it as a first order system in the following way

$$p = \mu\tau(h\eta - 1), \tag{58}$$

with  $\mu$  being a large positive parameter, and we introduce the evolution equation for  $\eta(t, x)$  which approximates the variable  $\tau(t, x) = 1/h(t, x)$ :

$$(h\eta)_t + (hu\eta)_x = hw,$$

with

$$(hw)_t + (huw)_x = -\frac{\mu}{\chi}(h\eta - 1).$$

The full system now reads

$$\begin{aligned} h_t + (hu)_x &= 0 \\ (hu)_t + (hu^2 + p_{tot})_x &= 0 \\ (h\eta)_t + (hu\eta)_x &= hw, \\ (hw)_t + (huw)_x &= -\frac{\mu}{\chi}(h\eta - 1). \end{aligned} \tag{59}$$

with the closure relation

$$p_{tot} = g\frac{h^2}{2} + \mu\tau(h\eta - 1) = g\frac{h^2}{2} + \mu(\eta - \tau). \tag{60}$$

The system is hyperbolic with the eigenvalues

$$\lambda_1 = \langle u \rangle - c, \quad \lambda_{2,3} = \langle u \rangle, \quad \lambda_4 = \langle u \rangle + c. \tag{61}$$

with

$$c^2 = gh + \mu\tau^2 \tag{62}$$

One can easily show that (59) are the Euler-Lagrange equations for the Lagrangian [12, 36]:

$$L = \int_{-\infty}^{+\infty} \left( \bar{h} \frac{\langle u \rangle^2}{2} - W(\bar{h}, \eta, \dot{\eta}) \right) dx,$$

with

$$W(\bar{h}, \eta, \dot{\eta}) = \frac{g\bar{h}^2}{2} - \frac{\chi\bar{h}\dot{\eta}^2}{2} + \frac{\mu h}{2} \left( \eta - \frac{1}{\bar{h}} \right)^2,$$

where, as usually, “dot” means the material derivative along the mean velocity  $\langle u \rangle$ . The pressure  $p_{tot}$  is defined as the partial Legendre transform with respect to  $h$  :

$$p_{tot} = h \frac{\partial W}{\partial h} - W = \frac{gh^2}{2} + \mu(\eta - \tau), \tag{63}$$

and the equation for  $\eta$  coming from two last equations of (59)

$$\ddot{\eta} + \frac{\mu}{\chi} (\eta - \tau) = 0 \quad (64)$$

is equivalent to the Euler-Lagrange equation for  $\eta$  :

$$\frac{\partial W}{\partial \eta} - \frac{\partial}{\partial t} \left( \frac{\partial W}{\partial \dot{\eta}} \right) - \frac{\partial}{\partial x} \left( \frac{\partial W}{\partial \dot{\eta}} \langle u \rangle \right) = 0. \quad (65)$$

In the limit  $\mu \rightarrow \infty$  we recover the original system, and, in particular, the total pressure  $p_{tot}$  becomes

$$p_{tot} = \frac{g\bar{h}^2}{2} - \chi \ddot{\tau}. \quad (66)$$

The interested reader can refer to [12, 36] and references therein for more details.

### 4.3 Numerical discretization

#### 4.3.1 Time stepping

*Elliptic-Hyperbolic approximation.* For system (56) we start from initial conditions simply set on physical quantities  $(h, u)$ . The system is then evolved in time by means of an explicit multistage method where, setting

$$U_{EH} = (h, hu)^T, \quad (67)$$

given the depth and velocities at time  $n$  and at intermediate stages  $(0, k)$ , as well as  $\phi^n, \dots, \phi^{k-1}$ , the generic stage  $k$  reads:

$$\begin{aligned} h^k \phi^k - \chi \left[ \frac{1}{h^k} (\phi^k - gh_x^k) \right]_x &= 0 \longrightarrow \phi^k \\ U_{EH}^{k+1} &= \sum_{\ell \geq 1} \alpha_\ell U_{EH}^{k+1-\ell} - \Delta t \sum_{\ell \geq 1} \beta_\ell \Psi_{SW}(U_{EH}^{k+1-\ell}, \phi^{k+1-\ell}), \end{aligned} \quad (68)$$

where  $\Psi_{SW}$  is a discrete approximation of the shallow water spatial residual, including the extra source  $\phi$ . In this approach we need to assemble and invert the elliptic operator at each intermediate stage. In one space dimension this is not a cumbersome operation (cf. next section), and could be avoided following the procedure proposed in [9], using the same Elliptic-Hyperbolic formulation but allowing one inversion per time step. In practice here we use (68) with two stages.

*Hyperbolic system.* In this case initial conditions are set on physical quantities  $(h, u)$  as well as the auxiliary variables  $w$  and  $\eta$  for which initial conditions are deduced from the limit  $\mu \rightarrow \infty$ :

$$\eta(0, x) = \tau(0, x), \quad w(0, x) = (u(0, x))_x / h(0, x).$$

For solitary waves, relations (41) and (47) have been used to evaluate these quantities.

System (59) is then can integrated in time using the efficient method proposed in [16]. In particular, setting

$$U_{Hyp} = (h, hu, h\eta, hw)^T, \quad (69)$$

given the solution value  $U_{Hyp}^n$  at time  $t^n$ , we use a classical second order Strang splitting method:

$$U_{Hyp}^{n+1} = O_1(\Delta t/2) O_{Hyp}(\Delta t) O_1(\Delta t/2)$$

where the operator  $O_1$  is the system of ODEs

$$\begin{aligned} \bar{h}_t &= 0 \\ (\bar{h}\langle u \rangle)_t &= 0 \\ (\bar{h}\eta)_t &= \bar{h} w, \\ (\bar{h}w)_t &= -\frac{\mu}{\chi} (\bar{h}\eta - 1). \end{aligned} \quad (70)$$

Given initial data  $(\tau_0, \langle u \rangle_0, \eta_0, w_0)$  the above is integrated exactly as

$$\begin{aligned}\eta &= \eta_0 \cos(\sqrt{\alpha}t) + \tau_0 (1 - \cos(\sqrt{\alpha}t)) + \frac{w_0}{\sqrt{\alpha}} \sin(\sqrt{\alpha}t) \\ w &= w_0 \cos(\sqrt{\alpha}t) - (\eta_0 - \tau_0)\sqrt{\alpha} \sin(\sqrt{\alpha}t)\end{aligned}\tag{71}$$

with  $\alpha = \mu/\chi$ .

The operator  $O_{\text{Hyp}}$  is nothing else than the hyperbolic homogenous part of system (59), which is integrated using a multi-stage method (with the same notation of (68))

$$U_{\text{Hyp}}^{k+1} = \sum_{\ell \geq 1} \alpha_\ell U_{\text{Hyp}}^{k+1-\ell} - \Delta t \sum_{\ell \geq 1} \beta_\ell \Psi_{\text{H}}(U_{\text{Hyp}}^{k+1-\ell}),\tag{72}$$

where  $\Psi_{\text{L}}$  is a discrete approximation of the right hand side of the homogenous hyperbolic system. In practice here we use a two stage method.

### 4.3.2 Discretization of the spatial differential operators

Spatial differential operators are approximated on a uniform discretization of the 1D spatial domain, with size  $\Delta x = 1/N$ ,  $N$  representing the number of mesh cells.

The elliptic operator in (68) is discretized with  $P^1$  finite elements, using the variational formulation (57). The invertibility of the resulting problem is characterized by proposition 1. In practice, the system being tri-diagonal, we have use Thomas method which allows to obtain the solution in two explicit seeps. The third derivative of  $h$  appearing in the right hand side is evaluated with a second order formula.

The hyperbolic operators, are discretized using a second order two-stages genuinely explicit Residual Distribution method [35, 1, 2]. To first order of accuracy in space one stage of the method can be written as

$$U_i^{k+1} = U_i^n - \frac{\Delta t}{\Delta x} \phi_i^{i-1/2}(U^n) - \frac{\Delta t}{\Delta x} \phi_i^{i+1/2}(U^n)\tag{73}$$

where the fluctuations  $\Phi_i^{i\pm 1/2}(U^n)$  are defined by some upwind biased distribution of the full residuals in mesh cells  $[x_{i-1}, x_i]$  and  $[x_i, x_{i+1}]$ . In particular, for a hyperbolic system reading

$$U_t + F_x = S, \quad A = F_U$$

we define

$$\phi^{i-1/2} = \int_{x_{i-1}}^{x_i} (F_x - S) = F_i - F_{i-1} - \Delta x(S_{i-1} + S_i)/2$$

and similarly for  $\Phi^{i+1/2}$ . With this definition we set here

$$\phi_i^{i-1/2} = \phi^{i-1/2}/2 + \tau A(U_{i-1/2})\phi^{i-1/2}, \quad \phi_i^{i+1/2} = \phi^{i+1/2}/2 - \tau A(U_{i+1/2})\phi^{i+1/2}\tag{74}$$

where the term multiplied by the matrix  $\tau$  is a stabilizing upwind bias, and  $U_{i\pm 1/2}$  denote simple the cell averages of the unknown. Classical upwinding is obtained for  $\tau = |A|^{-1}$ , Lax-Wendroff like schemes are obtained for  $\tau = \Delta t/2$ . This is the choice used here.

Instead of using a reconstruction, or more complex Lax-Wendroff like procedures [14, 9], a second order extension is built via a two-step procedure exploiting a first update to construct a strongly consistent residual. Given the first order predictor (73) we set  $(\cdot)^{n+1/2} = ((\cdot)^n + (\cdot)^{k+1})/2$ , and we compute in the second stage

$$\Phi^{i-1/2} = \frac{1}{\Delta t} \int_{t^n}^{t^{n+1}} \int_{x_{i-1}}^{x_i} (U_t + F_x - S) = \Delta x \frac{U_{i-1/2}^{k+1} - U_{i-1/2}^n}{\Delta t} + \frac{1}{2} \phi_i^{i-1/2}(U^n) + \frac{1}{2} \phi_i^{i-1/2}(U^{k+1})$$

and similarly for  $\Phi^{i+1/2}$ . The update is more simply written now in the form

$$U_i^{n+1} = U_i^{k+1} - \frac{\Delta t}{\Delta x} \Phi_i^{i-1/2} - \frac{\Delta t}{\Delta x} \Phi_i^{i+1/2}$$

where the split residuals are defined as in (74), with the obvious change of notation, and from which the form (68) and (72) can be easily deduced. The interested reader can refer to [35, 1, 2] and references therein for additional information, and theoretical aspects.

Finally, in the case of the elliptic-hyperbolic approximation the time step is computed from the shallow water part as

$$\Delta t = \nu \frac{\Delta x}{\max_i(|u_i| + \sqrt{gh_i})} \quad (75)$$

The interested reader can refer to [9, 17, 23] for Fourier analyses justifying this choice. For the fully hyperbolic approximation the source terms are exactly integrated in the splitting method, so we use the classical condition based on the largest eigenvalue

$$\Delta t = \nu \frac{\Delta x}{\max_i(|u_i| + \sqrt{gh_i + \mu\tau_i^2})}, \quad (76)$$

which shows a dependence on the value of the relaxation constant  $\mu$ .

## 5 Numerical tests

### 5.1 Verification on solitary waves

We have performed a verification of the one-dimensional solver using the solitary waves of section §3. We report here some of the results obtained allowing to validate the discretization and implementation part. Although other cases have been considered, we discuss here the case of a soliton of nonlinearity  $\epsilon = a\tau_\infty = 0.2$ , and we consider the case  $\chi = 0.4$  (cf. left picture on figure 3), and  $h_\infty = 1\text{m}$ .

On the spatial domain  $[-200, 200]\text{m}$  we have initialized the solution centering the solitary wave at  $x_0 = -100\text{m}$ , and let it travel for a distance  $L = 200\text{m}$ . We have solved the problem both using the elliptic-hyperbolic formulation, and the hyperbolic relaxation form, and performed a grid convergence study. The results are summarized on figure 5, in which the left pictures refer to the elliptic-hyperbolic formulation and the right ones to the fully hyperbolic one. Concerning the first approach, the results of the figure (and all our results) confirm a nice second order of convergence in all the norms for both depth and velocity.

For the hyperbolic reformulation, the results show a dependence on the value of the relaxation constant  $\mu$ . Already for  $\mu = 1000$  the error convergence passes from second to first, essentially due to the modelling errors. As the right picture on figure 5 shows, values of  $\mu$  at least of order  $10^4$  are necessary to correct this. However, such values impact negatively the computational time, due to the time step restriction (76).

To clarify the impact of this on the qualitative behaviour of the model, we have looked at the convergence in  $\mu$  of the solution at the final time. The results are summarized in figure 6. The left plot in the figure shows the wave profile of the numerically obtained soliton at final time. Despite what the error convergence suggests, clearly there is no visual difference in the solutions when using values of  $\mu$  above  $10^3$ . This may suggest that in practice such values may be enough. However a more general study, involving all possible values of  $\chi$ ,  $\epsilon$  and  $h_\infty$  would be necessary to confirm this. The right plot in the figure depicts the convergence of the depth wrt  $\mu$ , showing essentially a first order rate.

### 5.2 Breakdown of a Gaussian water column

We pass now to the study of the behaviour of the model. To begin with, we consider a simple case consisting in the breakdown of a Gaussian water column for which the initial state is given by

$$h(x, t = 0) = h_\infty(1 + \epsilon e^{-(x-x_0)^2/L^2}), \quad u(x, t = 0) = 0.$$

We start by investigating the propagation properties of the geometrical Green-Naghdi model proposed with respect to the parameters  $\chi$  and  $\epsilon$ . To this end we consider a battery of six cases corresponding to two values  $\chi = 0.1\text{m}^4$  and  $\chi = 0.6\text{m}^4$ , and three non-linearity values:  $\epsilon = 0.125$ ,  $\epsilon = 0.25$ , and  $\epsilon = 0.5$ . We consider a computational domain  $[-150, 150]\text{m}$ , on which we set the initial Gaussian centered in  $x_0 = 0$ , and we take  $L = 2\text{m}$ , and  $h_\infty = 2\text{m}$  as well. We simulate with both solution methods the evolution of the initial column up to time 16s using  $N = 10^4$  cells, and taking a value  $\mu = 10^3$  in the hyperbolic relaxation formulation.

The results are visualized on figure 7. Several remarks can be made. First of all, the two different implementations provide almost identical results, which is a further verification (albeit indirect) of our implementation. Second, comparing the left and right pictures, we can see that higher values of  $\chi$  result in longer waves, as one may expect since in this case the dispersive regularization has more weight. The lower value of  $\chi$  results in shorter and taller waves, with stronger and more localized secondary waves. These differences are enhanced when considering increasing values of non-linearity. Note that as the discussion of section §2.4 shows, for a given section shape, higher values of  $\chi$  may correspond both to deeper channels, as well as to larger ones. However note that large channels may fall out of the hypotheses of the model.

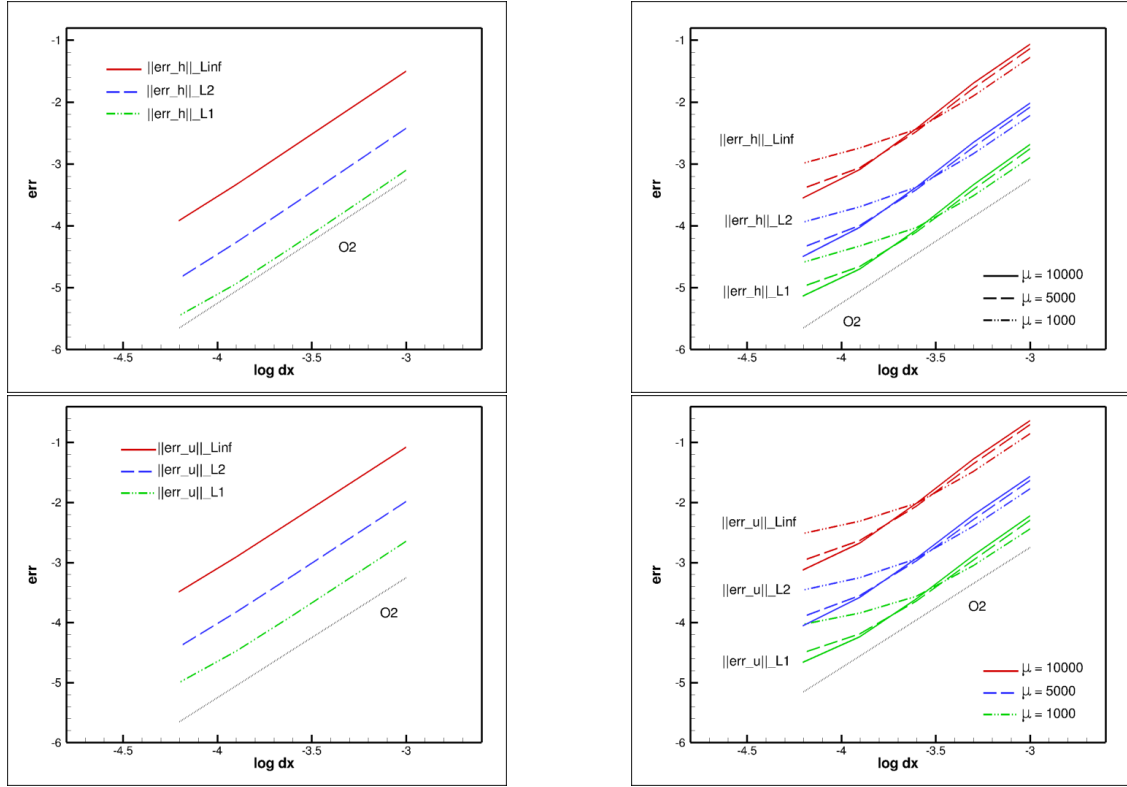


Figure 5: Solitary wave with  $a\tau_\infty = 0.2$  and  $\chi = 0.4$ : grid convergence. Left: elliptic-hyperbolic method. Right: hyperbolic reformulation with different values of  $\mu$ . Top: water height  $\bar{h}$ . Bottom: averaged velocity.

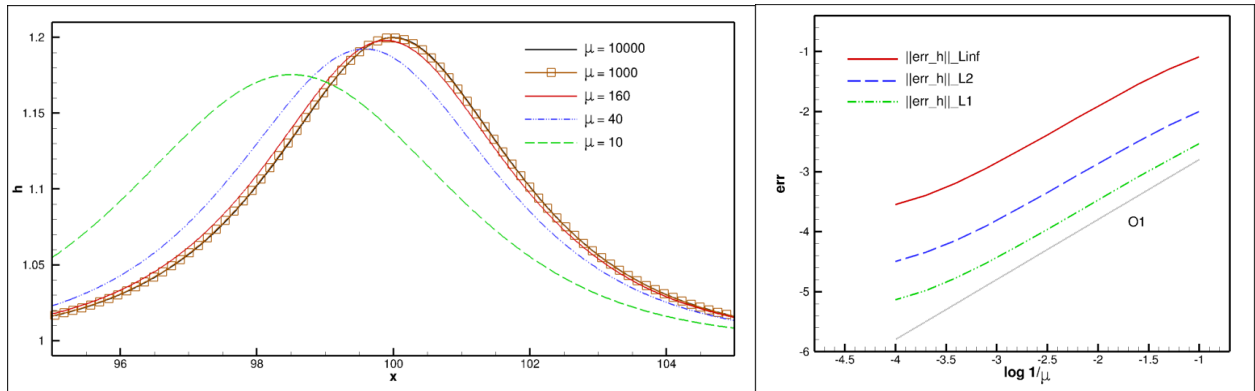


Figure 6: Solitary wave with  $a\tau_\infty = 0.2$  and  $\chi = 0.4$ : convergence with  $\mu$  for the hyperbolic reformulation. Left: depth distribution at final time. Right: error convergence.



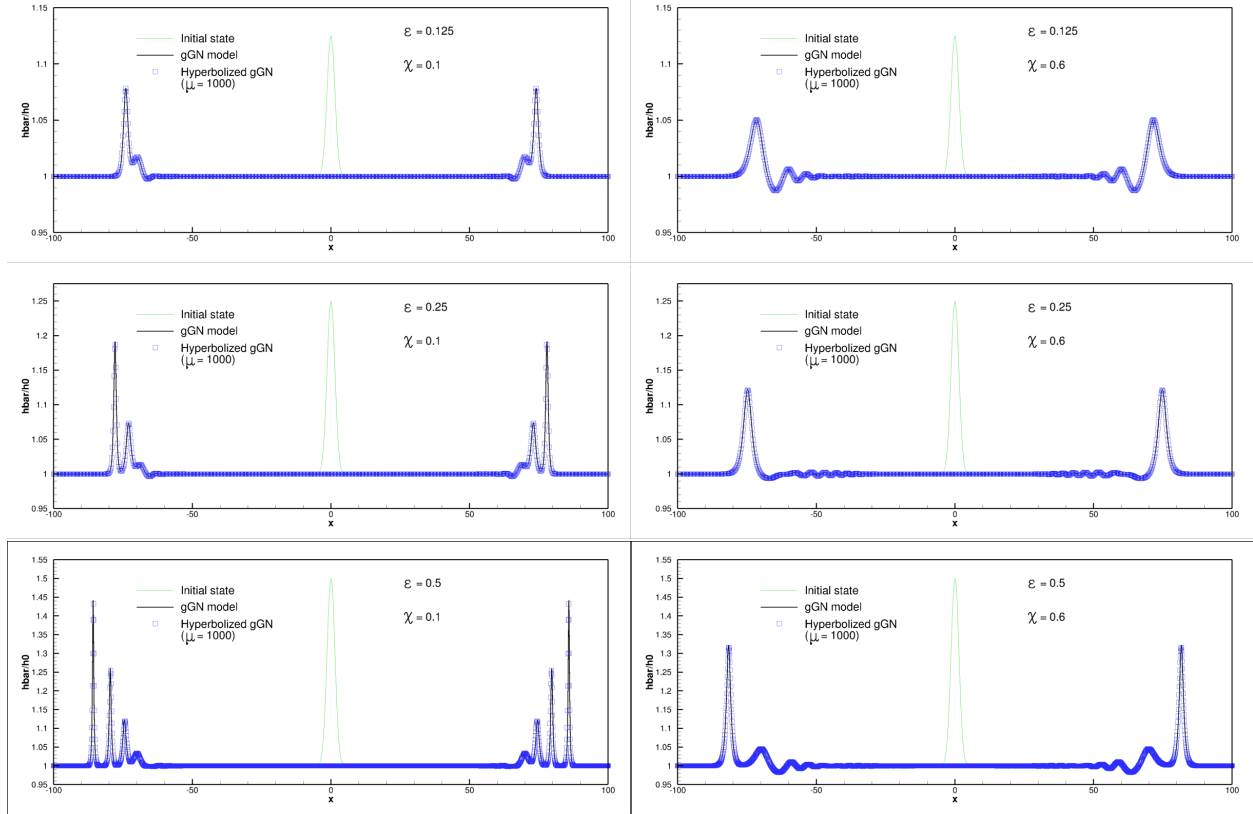


Figure 7: Breakdown of a Gaussian water column: solutions at time  $t = 16$ s for three values of the non-linearity coefficient  $\epsilon = a\tau_\infty \in \{0.125, 0.25, 0.5\}$ . Left column:  $\chi = 0.1\text{m}^4$ . Right column  $\chi = 0.6\text{m}^4$ .

### 5.2.1 Validation against section averaged 2D shallow water simulations

Since for this case there is no exact solution, we will consider a validation against section averaged full 2D shallow water computations. The latter have been run with the solver developed in the series of works [34, 3, 4], and thoroughly validated on a wide range of cases against analytical and experimental data.

The setup of the 2D simulations is the following. We consider three sections: symmetric trapezoidal; symmetric triangular; non-symmetric trapezium. Following the notation of section §2, we set for the case  $\chi = 0.1\text{m}^4$   $b_0 = 2.5\text{m}$ , and we then for each section we choose appropriate values of the remaining lengths. In particular we take  $(\ell_1, \ell_2, \ell_3) = (1.07, 0.36, 1.07)\text{m}$  in the symmetric trapezoidal case, and  $(\ell_1, \ell_2, \ell_3) = (1.38575, 0.0, 1.38575)\text{m}$  in the triangular one. For the non-symmetric trapezium we choose  $(\ell_1, \ell_2, \ell_3) = (1.284, 0.36, 0.7249)\text{m}$ . For  $\chi = 0.6\text{m}^4$  we have set  $b_0 = 2.75\text{m}$ , and chosen  $(\ell_1, \ell_2, \ell_3) = (2.165, 1.1175, 2.165)\text{m}$  in the trapezoidal case, and  $(\ell_1, \ell_2, \ell_3) = (3.0855, 0.0, 3.0855)\text{m}$  in the triangular one. Also in this case we have computed solutions with a non symmetric trapezoidal section with  $(\ell_1, \ell_2, \ell_3) = (2.598, 1.1175, 1.14668)\text{m}$ .

In all cases, the initial solution is then set using equation (6):

$$h(x, y, t = 0) = \bar{h}(x, t = 0) - b(y) + \bar{b} = h_\infty(1 + \epsilon e^{-(x-x_0)^2/L^2}) - b(y) + \bar{b}.$$

with  $b(y)$  defined as in figure 1m and  $h_\infty = 2\text{m}$ . Only the case  $\epsilon = 0.25$  is commented for brevity. The computational domain is the rectangle  $[-150, 150]\text{m} \times [-\ell_1 - \ell_2/2, \ell_2/2 + \ell_3]\text{m}$ . Both velocity components are set to zero at  $t = 0$ , and reflective boundary conditions are set on all boundaries. With the above initialization, and the chosen values for  $h_\infty$  and  $b_0$ , we satisfy all the hypotheses of the model, including the fact that the minimum depth at initialisation is well above zero, which also avoids the activation of wet/dry treatments. Fine triangulations with mesh sizes  $\Delta x \approx 6.25\text{cm}$  and  $\Delta y \approx 2\text{cm}$  are used. As a first step, we run a case with  $b(y) = 0$ . The result is reported for completeness on figure 8 showing the expected behaviour from the shallow water system with shock formation in finite time. The right plots in the figure show  $y$ -averaged data confirming this behaviour.

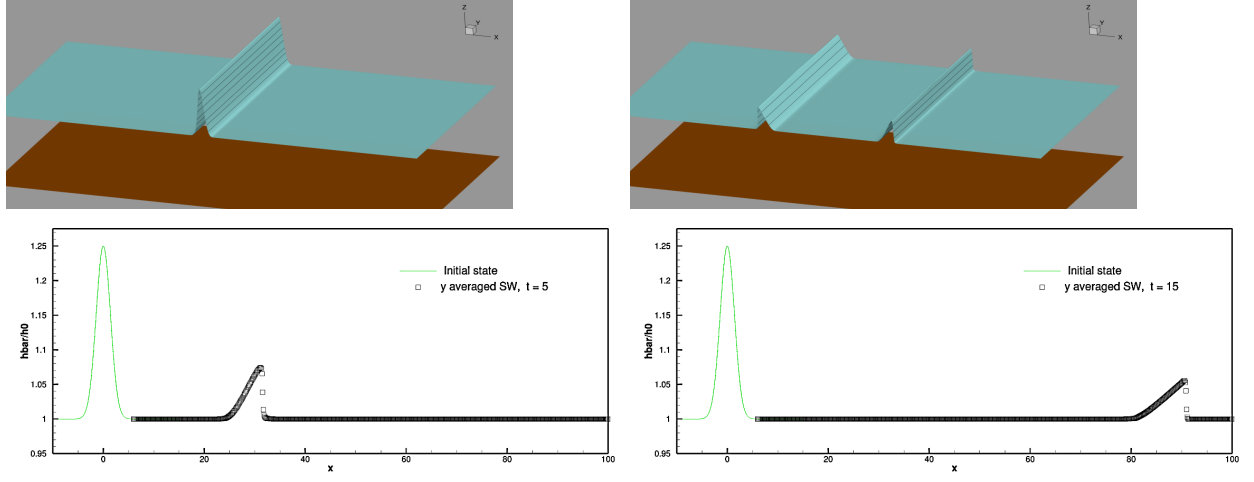


Figure 8: Breakdown of a Gaussian water column. Free surface from shallow water simulations corresponding to  $\epsilon = 0.25$ . Initial solution (top-left), and solution at time  $t = 5$ s (top-right). Bottom:  $y$ -averaged data at times  $t = 5$ s (left) and  $t = 15$ s (right).

We now consider the simulations including bathymetric variations. three dimensional visualizations are reported on figures 9 for the case  $\chi = 0.1\text{m}^4$ , and 10 for  $\chi = 0.6\text{m}^4$ . To save space a zoom of the right-going waves is shown, but the results are almost exactly symmetric wrt the  $y$  axis.

The figures clearly show the formation and propagation of smooth waves, with roughly a first wave resembling to a soliton with variable amplitude along  $y$ , followed by secondary smooth waves. The first wave amplitudes are higher on the shallower parts than in the center. These results are similar to those presented in [10] for Favre waves: no discontinuities are produced despite the nonlinear hyperbolic character of the system. Comparing the two values of  $\chi$  we can see that for  $\chi = 0.1\text{m}^4$  (thinner/shallower channels) we obtain shorter waves, with secondary ones clustered close to the first one. For higher  $\chi$  we can clearly see more dispersion, with longer waves and secondary waves with lower celerity. This behaviour is identical to the one observed in one dimension for the gGN system.

To go further, we now compute numerically  $y$ -averages of the 2D data, and compare them to the solutions obtained with the geometrical Green-Naghdi equations developed in this paper, which for the value of  $\epsilon = 0.25$  correspond to the second row of figure 7. The comparisons are reported in figure 11. The plots show that the averaged data for the different sections are very close and present an excellent match with the solutions of the 1D gGN model. A somewhat larger difference is observed for the non-symmetric case which clearly presents a more three dimensional wave field, with more secondary waves perhaps missed by our approximate model. The agreement is however generally in favor of the new model. The results above are in line with those reported in [10] for Favre waves in trapezoidal channels, and further confirm the existence of these dispersive-like waves due to transverse refraction. These are indeed dispersive waves, which can be modelled with the section averaged geometrical Green-Naghdi equations proposed in this paper.

### 5.3 Riemann problem

We consider now the computation of Riemann problems. As in [36, 33] we consider a smoothed initial discontinuity:

$$h((x, t = 0)) = h_0^{\text{ID}}(x) = h_0 \left(1 + \frac{\epsilon}{2} (1 - \tanh x)\right), \quad u(x, t = 0) = 0.$$

As done for the column fall, we will start by comparing the two reformulations of the model for different values of the parameters. We will consider here three values of the non-linearity  $\epsilon = 0.125$ ,  $\epsilon = 0.25$ , and  $\epsilon = 0.5$ , and again the values of the dispersion coefficient  $\chi = 0.1\text{m}^4$ , and  $\chi = 0.6\text{m}^4$ . We compute mesh converged numerical solutions for both approaches discussed in section §4, using a value  $\mu = 10^3$  for the hyperbolized formulation. The results are summarized on figure 12. The plots show that the two formulations give almost identical results, except for the highest values of the non-linearity for which the hyperbolized model provide slightly lower peaks and a small phase shift. This effect, visible on figure 13, is most certainly due to the finite value of  $\mu = 10^3$  chosen.

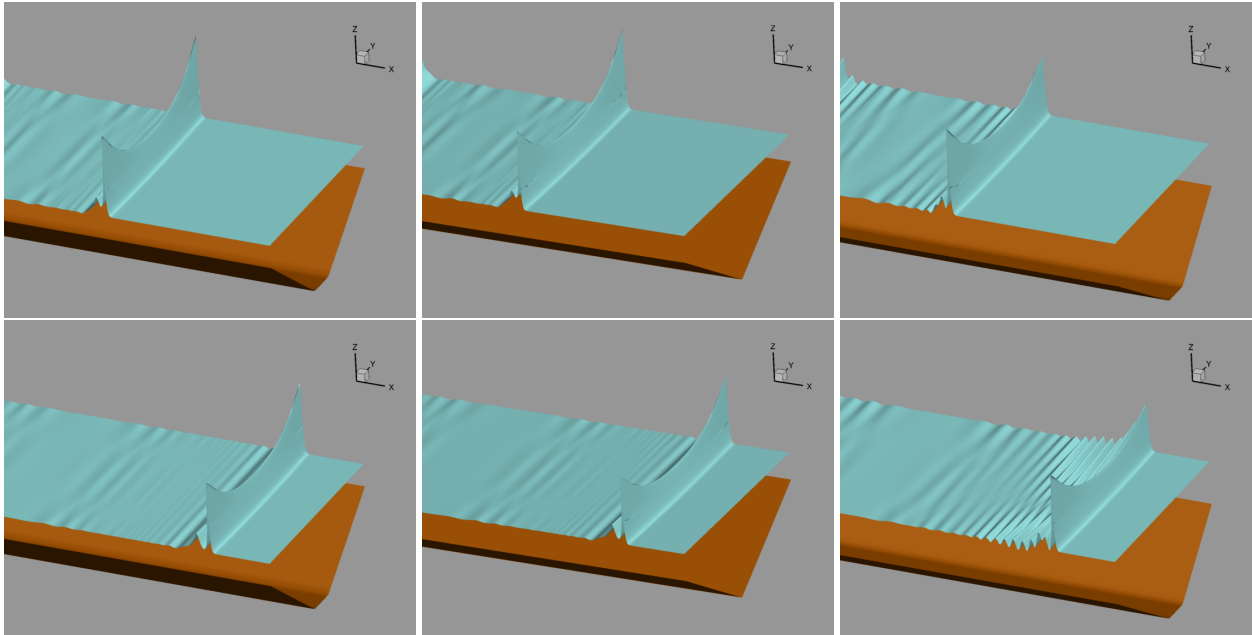


Figure 9: Breakdown of a Gaussian water column: view of the right-going wave. Shallow water simulations on bathymetric sections corresponding to  $\chi = 0.1\text{m}^4$  and  $\epsilon = 0.25$ . Times  $t = 8\text{s}$  (top), and  $t = 16\text{s}$  (bottom). Trapezoidal (left), triangular (center), and asymmetric trapezoidal (right) sections.

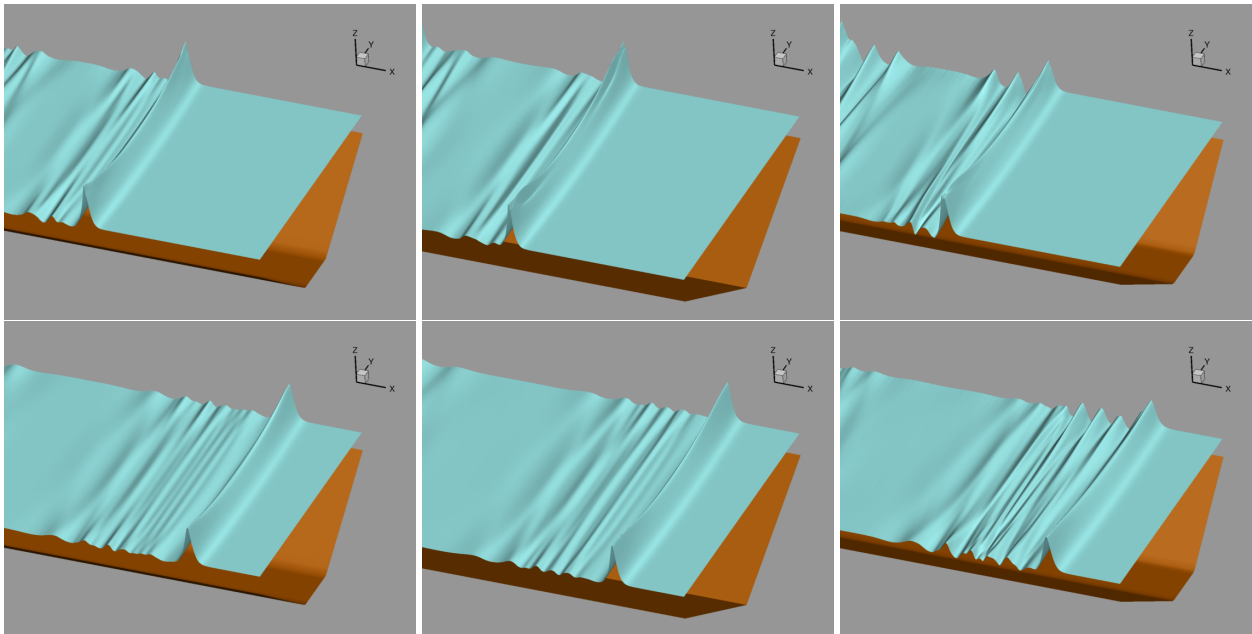


Figure 10: Breakdown of a Gaussian water column: view of the right-going wave. Shallow water simulations on bathymetric sections corresponding to  $\chi = 0.6\text{m}^4$  and  $\epsilon = 0.25$ . Times  $t = 8\text{s}$  (top), and  $t = 16\text{s}$  (bottom). Trapezoidal (left), triangular (center), and asymmetric trapezoidal (right) sections.

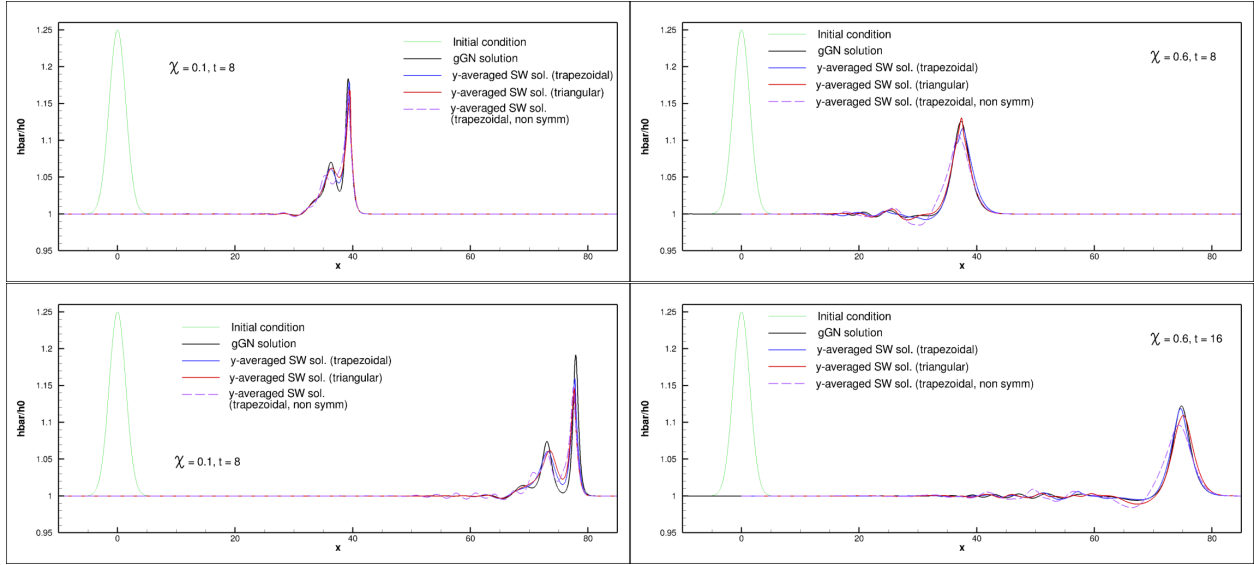


Figure 11: Breakdown of a Gaussian water column. Comparison of width averaged solutions from shallow water simulations with solutions of the gGN model. Left :  $\chi = 0.1\text{m}^4$ . Right :  $\chi = 0.6\text{m}^4$ . Solutions at time  $t = 16\text{s}$ .

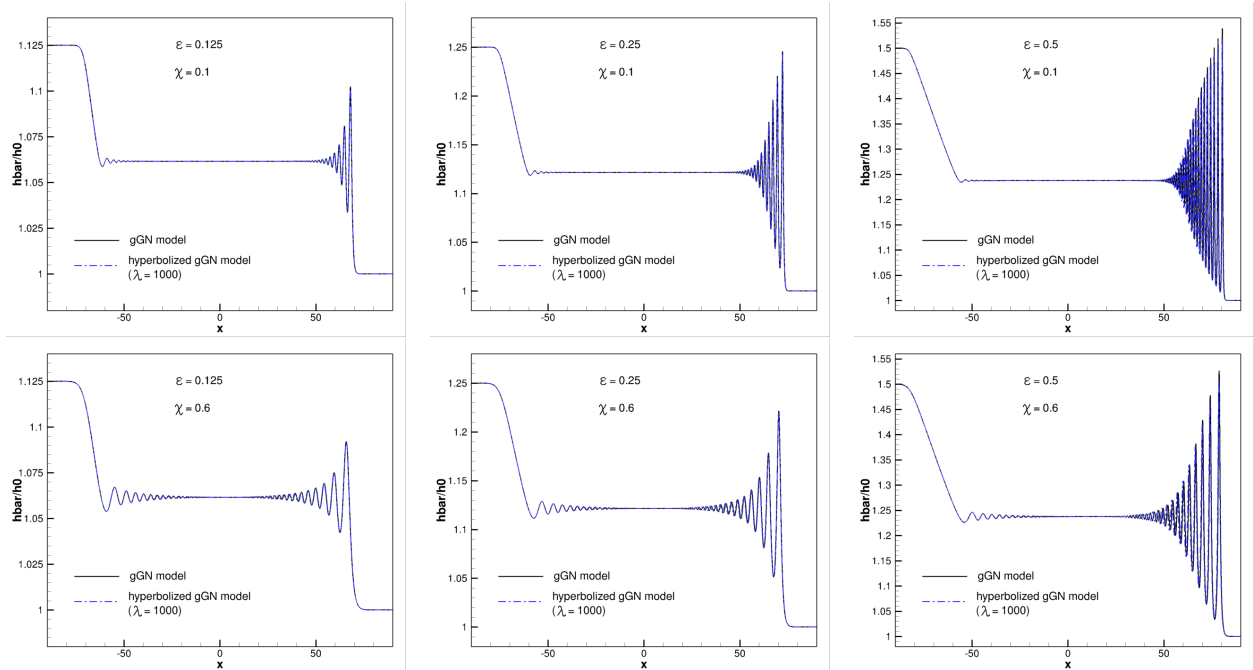


Figure 12: Riemann problem. Comparison of solutions at  $t = 15\text{s}$  for the gGN solutions using the elliptic-hyperbolic and hyperbolic relaxation for  $\epsilon = 0.125$  (left column),  $\epsilon = 0.25$  (central column),  $\epsilon = 0.5$  (right column), and with  $\chi = 0.1\text{m}^4$  (top), and  $\chi = 0.6\text{m}^4$  (bottom).

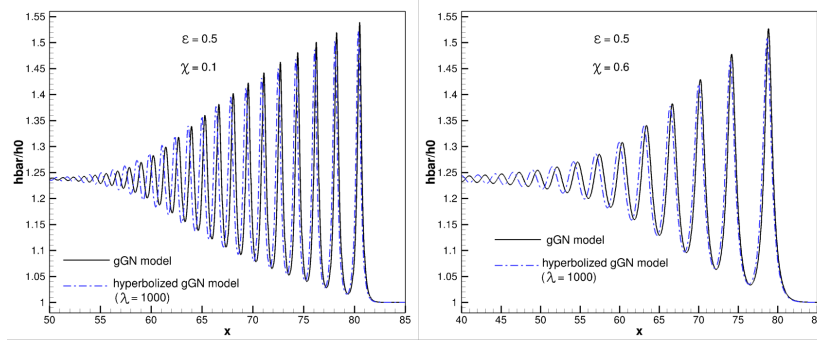


Figure 13: Riemann problem. Zoom of the leading waves for  $\epsilon = 0.5$ .

Concerning the qualitative behaviour of the model, as expected, smaller values of  $\chi$  correspond to very small dispersive regularizations and provide higher frequency dispersive shocks. Similarly, higher nonlinearities lead to stronger secondary waves, all travelling faster, and ultimately also dispersive shocks with shorter wavelengths at this final time.

### 5.3.1 Validation against section averaged 2D shallow water simulations

As done for the previous case, as a means of validation we have run full 2D shallow water computations. We proceed as before. We consider equivalent sections providing values of the geometrical dispersion coefficient  $\chi = 0.1\text{m}^4$ , and  $\chi = 0.6\text{m}^4$ . The geometrical definitions are the same of section §5.2.1. Then we initialize the solution based on relation (6):

$$h(x, y, t = 0) = h_0^{\text{1D}}(x) - b(y) + \bar{b},$$

with  $h_0^{\text{1D}}(x)$  defined above. As before, with these values we can initialize the flow on a constant upstream average depth of 2m, without incurring in dry areas. We will consider here the case with lowest non-linearity  $\epsilon = 0.125$ .

To begin with, we look at the free surface obtained at  $t = 15\text{s}$ , which are reported on figure 14. The first thing we can see, is that none of the computations with bathymetry exhibits the formation of classical shock waves, as in the flat bathymetry results reported in the bottom picture for completeness. All the results show a free surface level which has an almost one dimensional phase, with finite wavelength oscillations. These wavelengths are several orders of magnitude larger than the mesh size, and have nothing to do with numerical dispersion, or lack of monotonicity, but are related to dispersion induced by physical refraction in the  $y$  direction. We can not that for a given  $\chi$ , equivalent sections provide very close results to one another, with perhaps the main difference between the symmetric and non-symmetric shapes. The latter ones give a more three dimensional field, richer in secondary waves. As for the water column case, the more shallow the flow, the larger the wave heights. Also here we can clearly observe, as in one dimensions, more dispersive behaviour for larger  $\chi$ : the waves are longer, and so is disparity in celerity also larger.

To validate the gGN model, we compare its results with transverse averages of the 2D solutions. The resulting comparison is reported on figure 15. All the comparisons show a nice agreement. For both values of  $\chi$  the symmetric 2D results provide a solution with 4 or 5 peaks, while the 1D model predicts in general more secondary oscillations. The amplitude and phases of the leading front are excellent, and those of the first two secondary waves also in general captured nicely by the gGN model. The average non-symmetric results show in general slightly longer waves, which may originate from the merging of more secondary waves in this short time scale simulation.

Overall these results, as those of the previous section, validate our model, showing a very satisfactory agreement. We also confirm the findings of [10] on more simulations, and highlight the existence of these little known dispersive-like waves due to transverse refraction, which can be modelled with our geometrical Green-Naghdi equations.

### 5.3.2 Soliton fission

To conclude the study of the Riemann problem, we have run 1D simulations for largest values  $\chi = 0.6\text{m}^4$  and  $\epsilon = 0.5$  for a much longer time  $t = 600\text{s}$ , in order to verify the occurrence of soliton fission, and compare the resulting solitons with the ones studied in sections §3.3 and §5.1. We report in figure 16 a visualization of the front of the wave superposing several instances of the leading waves. In the visualizations, we follow second peak of the dispersive front, so that we may visualize the separation of the first soliton. For the last instance, we have measured an amplitude  $a = 0.56h_\infty$  which we used to generate a corresponding exact gGN soliton solving (44) with matching amplitude.

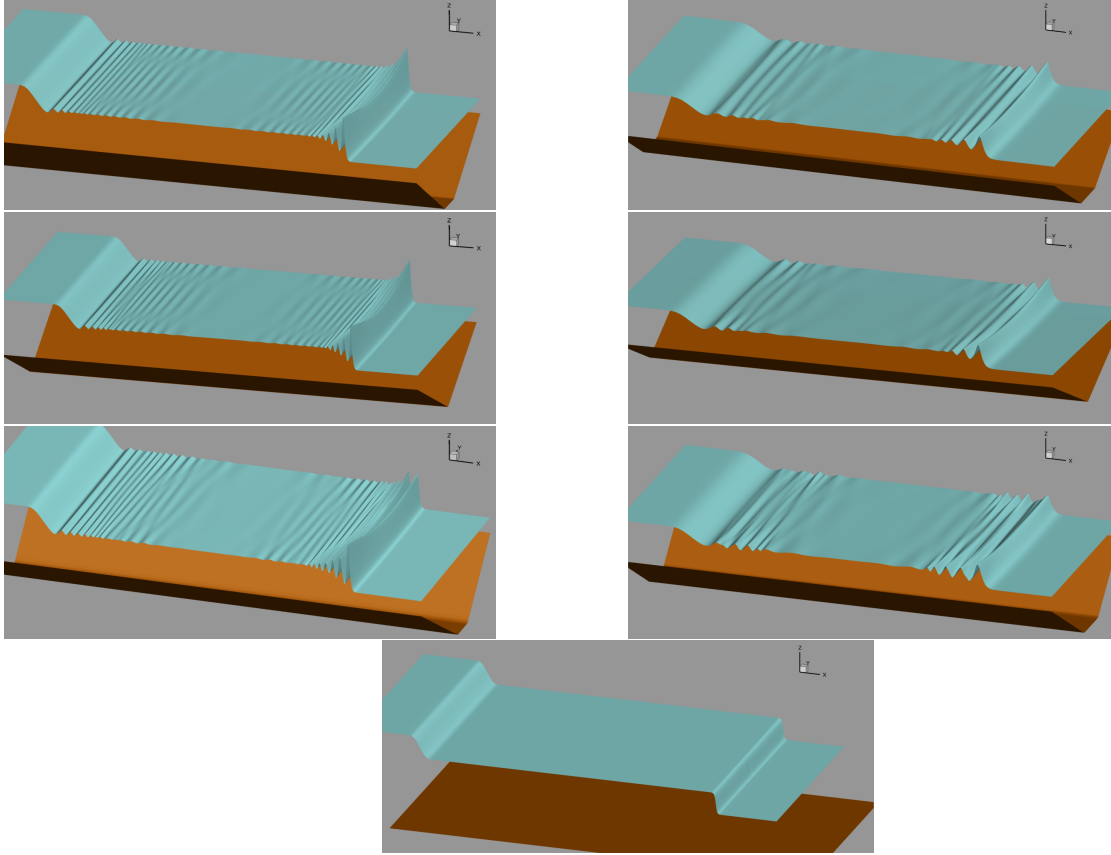


Figure 14: Riemann problem. Free surface from shallow water solutions at  $t = 15$ s for  $\epsilon = 0.125$  with trapezoidal (left column) and triangular (right column) sections corresponding to  $\chi = 0.1\text{m}^4$  (first row), and  $\chi = 0.6\text{m}^4$  (second row). The last row shows the result for flat bathymetry.

The exact soliton corresponding to the measured amplitude is reported in green in the picture, such that its maximum is superposed to the first soliton resulting from the Riemann problem. The agreement is excellent.

#### 5.4 Composite solution

Finally, we consider the composite travelling solution of section §3.4. Our objective is to understand if the model indeed admits stable solutions as those derived. So, as a first exercise, we perform a grid convergence study. We start from the initial solution with values provided at the end of §3.4 (cf figure 4), using the regularization with half gGN soliton. Simulations are run on the computational domain  $[-100, 2300]\text{m}$ , with the initial jump at the origin. Free boundary conditions are imposed on the right, while the constant solution is imposed on the left. We let the model evolve the flow for 50s, and then compare with the initial solution translated by the exact celerity  $D$  computed analytically. The results are reported on figure 17.

To give a more general view, the figure reports both the solutions in the subdomain  $[-100, 1000]\text{m}$ , and zoom of the first peaks, including the regularized one. As one can see, both numerical approximations of the model converge nicely to the travelling solution. The difference between the original and hyperbolic reformulation is well explained by the finite value of  $\mu$ . Quite interestingly, the results converge to the translated initial solution, including the regularization. This suggests that the actual solution admitted is composed from a constant state, obtained from the Rankine-Hugoniot relations, and an infinite series of oscillations between the values  $\tau_1$  and  $\tau_2$ , much resembling an infinite series of solitary waves propagating at the level  $\tau_2$ .

To get a better insight on the impact of the initialization, we have performed the same simulation with the different treatments of the “jump” discussed in section §3.4. Grid converged results are reported on figure 18. We can say several things. Firstly, past the regularized peak the three cases provide an identical infinite train of waves. Secondly, the initialization with a half soliton is the only one which does not introduce any secondary waves, and is simply

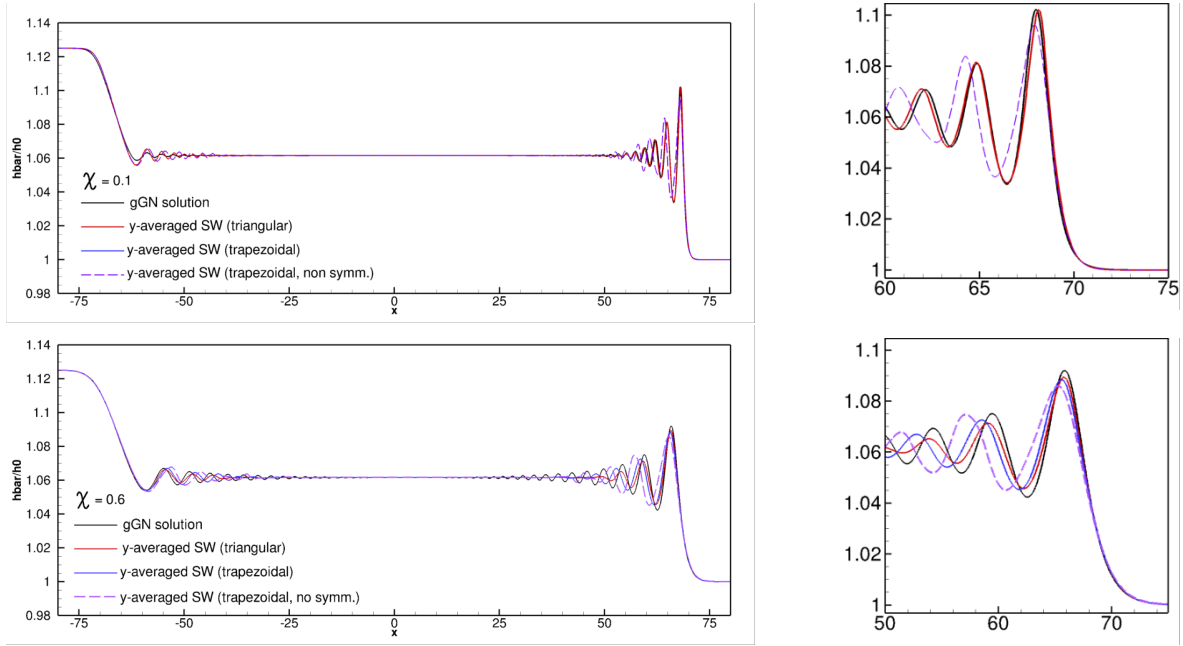


Figure 15: Riemann problem. Comparison of averaged free surface profiles at  $t = 15$ s for  $\epsilon = 0.125$ , and  $\chi = 0.1\text{m}^4$  (first row), and  $\chi = 0.6\text{m}^4$  (second row). Geometrical Green-Naghdi model compared to transversely averaged 2D shallow water computations. Left: overall view. Right: zoom of the leading waves.

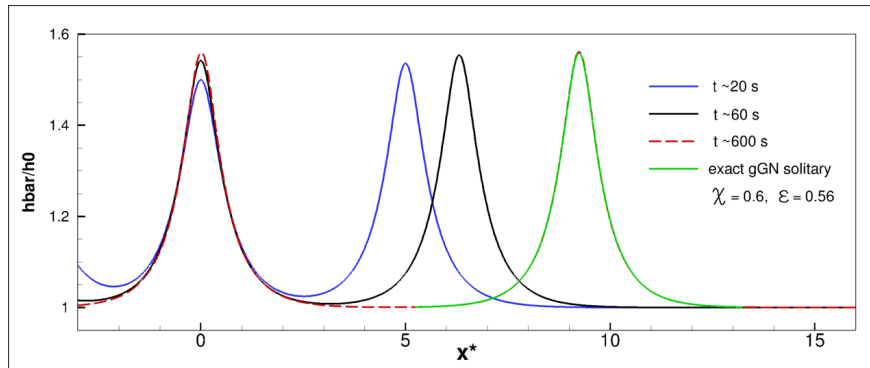


Figure 16: Riemann problem: soliton fission for the case  $\epsilon = 0.5$ , and  $\chi = 0.6\text{m}^4$ . Solutions at times  $t = 20$ s (blue),  $t = 60$ s (black), and  $t = 600$ s (red). All solutions translated to have the second peak at the origin. The last solution is used to generate a corresponding exact gGN soliton (in green) obtained solving (44) with matching amplitude.



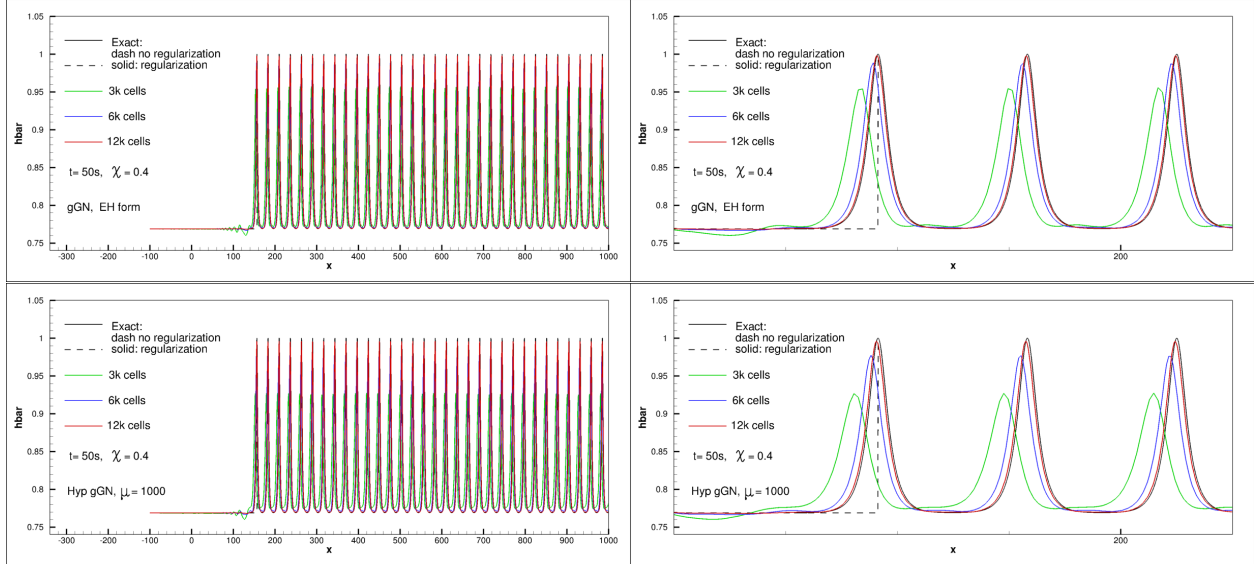


Figure 17: Composite solution. Grid convergence using toward the advected regularized solution (using the gGN half soliton) of figure 4 at  $t = 50s$ , using  $\chi = 0.4m^4$ ,  $\tau_1 = 1m^{-1}$ ,  $\tau_2 = 1.3m^{-1}$ , and  $\tau_3 = 1.301m^{-1}$ . Top: original gGN model with elliptic-hyperbolic approximation. Bottom: hyperbolic model with  $\mu = 1000$ . Left: overview of the solution in the subdomain  $[-100, 1000]m$ . Right: first three peaks (including regularized jump).

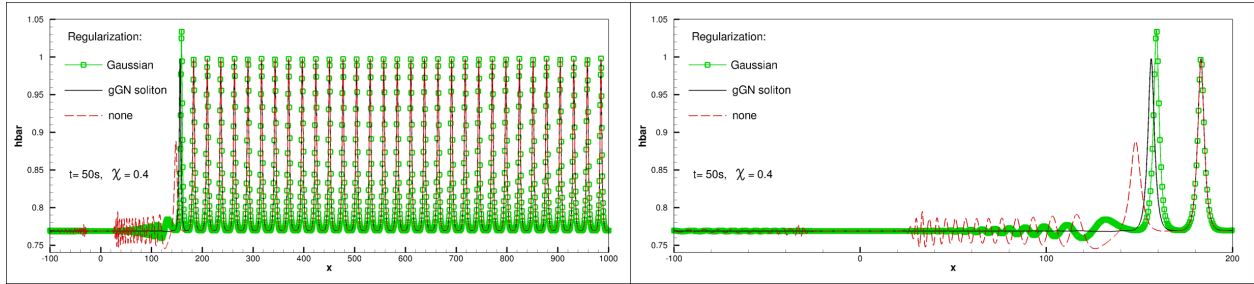


Figure 18: Composite solution: influence of the regularization of the initial solution.

propagated by the model. This indicates that the exact solution is not a discontinuous one in a classical sense, but rather a composite solution composed of a constant state  $\star$ , and a periodic wave train of waves of large length. This traveling wave solution verifies the generalized Rankine-Hugoniot conditions coming from the mass and momentum equations. In this sense, it is a “discontinuous” solution of the gGN equations. The relation of such “discontinuous” solutions with shock solutions of the corresponding Whitham system can be established (see such a study in [20] for the Benjamin-Bona-Mahony equation having the same dispersive properties as the gGN system).

## 6 Conclusion

From the two-dimensional hyperbolic non-linear shallow water equations we have derived a one-dimensional dispersive model (geometrical Green-Naghdi type (gGN) model) for averaged the averaged depth and velocity. The dispersive effects arise from transverse diffraction due to bathymetric variations. These waves were studied first in [10] in the context of undular bore propagation in channels. The model has several appealing properties: it admits an energy conservation law, exact travelling waves solutions, a dispersion relation close to the one of [10] which has shown to provide correct quantitative predictions of the wavelengths of undular bores for low Froude numbers.

We have suggested and implemented two approaches to solve the model numerically, and provided ample validation of our implementation. In particular, we have shown by means of genuinely 2D shallow water simulations the occurrence of these dispersive-like waves, adding evidence to the one already presented in [10]. Moreover, performing section averages of these multi dimensional computations we have been able to validate the geometrical gGN model proposed.



This study goes one step further compared to previous ones, however many questions remain open concerning e.g. the ranges in which the dispersive waves actually occur. There is certainly some the interaction between non-linearity and dispersion which controls this process, and probably an equivalent of wave breaking range in which the shallow water equations do predict shock formation. Another issue open is the management of the banks, which has been left out of this work, and the formulation of a model including both horizontal dispersion (dispersive-like waves), and vertical as the classical Serre-Green-Naghdi model.

## Acknowledgements

SG would like to thank the Isaac Newton Institute for Mathematical Sciences, Cambridge, for support and hospitality during the programme "Emergent phenomena in nonlinear dispersive waves", where work on this paper was undertaken. This work was supported by EPSRC grant EP/R014604/1. MR is a member of the CARDAMOM research team of the Inria center at University of Bordeaux.

## References

- [1] R. Abgrall and M. Ricchiuto. High order methods for CFD. In Rene de Borst Erwin Stein and Thomas J.R. Hughes, editors, *Encyclopedia of Computational Mechanics, Second Edition*. John Wiley and Sons, 2017.
- [2] Rémi Abgrall and Mario Ricchiuto. *Hyperbolic Balance Laws: Residual Distribution, Local and Global Fluxes*, pages 177–222. Springer Nature Singapore, Singapore, 2022.
- [3] Luca Arpaia and Mario Ricchiuto.  $r$ - adaptation for shallow water flows: conservation, well balancedness, efficiency. *Computers & Fluids*, 160:175–203, 2018.
- [4] Luca Arpaia and Mario Ricchiuto. Well balanced residual distribution for the ALE spherical shallow water equations on moving adaptive meshes. *J.Comput.Phys.*, 405, 2020.
- [5] N. Bonneton, P. Bonneton, J.-P. Parisot, A Sottolichio, and G Detandt. Tidal bore and Mascaret - example of Garonne and Seine Rivers. *Comptes Rendus Geosciences*, 344(508-515), 2012.
- [6] P. Bonneton, N. Bonneton, J.-P. Parisot, and B. Castelle. Tidal bore dynamics in funnel-shaped estuaries. *Journal of Geophysical Research: Oceans*, 120(2):923–941, 2015.
- [7] Philippe Bonneton, Florent Chazel, David Lannes, Fabien Marche, and Marion Tissier. A splitting approach for the fully nonlinear and weakly dispersive Green–Naghdi model. *J.Comput.Phys*, 230(4):1479–1498, 2011.
- [8] S. Busto, M. Dumbser, C. Escalante, N. Favrie, and S. Gavrilyuk. On High Order ADER Discontinuous Galerkin Schemes for First Order Hyperbolic Reformulations of Nonlinear Dispersive Systems. *Journal of Scientific Computing*, 87, 2021.
- [9] Aurore Cauquis, Mario Ricchiuto, and Philippe Heinrich. Lax–wendroff schemes with polynomial extrapolation and simplified lax–wendroff schemes for dispersive waves: A comparative study. *Water Waves*, pages 1–33, 2022.
- [10] R. Chassagne, A.G. Filippini, M. Ricchiuto, and P. Bonneton. Dispersive and dispersive-like bores in channels with sloping banks. *Journal of Fluid Mechanics*, 870:595–616, 2019.
- [11] Rémi Chassagne, Andrea Gilberto Filippini, Mario Ricchiuto, and Philippe Bonneton. Dispersive and dispersive-like bores in channels with sloping banks. Research Report RR-9228, Inria Bordeaux Sud-Ouest, 2018.
- [12] Firas Dhaouadi, Nicolas Favrie, and Sergey Gavrilyuk. Extended Lagrangian approach for the defocusing nonlinear Schrödinger equation. *Studies in Applied Mathematics*, 142(3):336–358, 2019.
- [13] Vincent Duchêne. Rigorous justification of the favrie–gavrilyuk approximation to the serre–green–naghdi model. *Nonlinearity*, 32(10):3772, sep 2019.
- [14] Michael Dumbser, Dinshaw S. Balsara, Eleuterio F. Toro, and Claus-Dieter Munz. A unified framework for the construction of one-step finite volume and discontinuous galerkin schemes on unstructured meshes. *J.Comput.Phys.*, 227(18):8209–8253, 2008.
- [15] H. Favre. *Etude théorique et expérimentale des ondes de translation dans les canaux découverts*. Dunod, 1935.
- [16] N Favrie and S Gavrilyuk. A rapid numerical method for solving Serre-Green-Naghdi equations describing long free surface gravity waves. *Nonlinearity*, 30(7):2718, 2017.
- [17] Andrea Gilberto Filippini, Maria Kazolea, and Mario Ricchiuto. A flexible genuinely nonlinear approach for nonlinear wave propagation, breaking and run-up. *J.Comput.Phys.*, 310:381–417, 2016.

- [18] Sergey Gavriluk. Multiphase flow modeling via hamilton’s principle. In Francesco dell’Isola and Sergey Gavriluk, editors, *Variational Models and Methods in Solid and Fluid Mechanics*, pages 163–210. Springer Vienna, Vienna, 2011.
- [19] Sergey Gavriluk, Boniface Nkonga, Keh-Ming Shyue, and Lev Truskinovsky. Stationary shock-like transition fronts in dispersive systems. *Nonlinearity*, 33(10):5477, 2020.
- [20] Sergey Gavriluk and Keh-Ming Shyue. Singular solutions of the BBM equation: analytical and numerical study. *Nonlinearity*, 35(1):388, nov 2021.
- [21] Sergey Gavriluk and Keh-Ming Shyue. 2D Serre-Green-Naghdi equations over topography: Elliptic operator inversion method. *Journal of Hydraulic Engineering*, 150(1), 2024.
- [22] B. Jouy, D. Violeau, M. Ricchiuto, and M. Le. One dimensional modelling of favre waves in channels. *Applied Mathematical Modelling*, 133:170–194, 2024.
- [23] M. Kazolea, A.G. Filippini, and M. Ricchiuto. Low dispersion finite volume/element discretization of the enhanced green–naghdi equations for wave propagation, breaking and runup on unstructured meshes. *Ocean Modelling*, 182:102157, 2023.
- [24] D. Ketcheson and M. Quezada de Luna. Diffractons : Solitary Waves Created by Diffraction in Periodic Media. *Multiscale Modeling & Simulation*, 13(1):440–458, January 2015.
- [25] David I. Ketcheson, Lajos Lóczi, and Giovanni Russo. A multiscale model for weakly nonlinear shallow water waves over periodic bathymetry, 2023.
- [26] O. Le Métayer, S. Gavriluk, and S. Hank. A numerical scheme for the green–naghdi model. *J.Comput.Phys.*, 229(6):2034–2045, 2010.
- [27] R. Lemoine. Notules hydrauliques. *La Houille Blanche*, (2):183–186, March 1948.
- [28] D. I. Ketcheson M. Quezada de Luna. Solitary water waves created by variations in bathymetry. *Journal of Fluid Mechanics*, 917, May 2021.
- [29] Alireza Mazaheri, Mario Ricchiuto, and Hiroaki Nishikawa. A first-order hyperbolic system approach for dispersion. *J.Comput.Phys.*, 321:593–605, 2016.
- [30] Victor Michel-Dansac, Pascal Noble, and Jean-Paul Vila. Consistent section-averaged shallow water equations with bottom friction. *Eur.J.Mech. - B/Fluids*, 86, 2021.
- [31] M. Parisot. Entropy-satisfying scheme for a hierarchy of dispersive reduced models of free surface flow. *International Journal for Numerical Methods in Fluids*, 91(10):509–531, 2019.
- [32] Manuel Quezada de Luna and David I. Ketcheson. Two-dimensional wave propagation in layered periodic media. *SIAM Journal on Applied Mathematics*, 74(6):1852–1869, 2014.
- [33] Hendrik Ranocha and Mario Ricchiuto. Structure-preserving approximations of the serre-green-naghdi equations in standard and hyperbolic form, 2024.
- [34] M. Ricchiuto. An explicit residual based approach for shallow water flows. *J.Comput.Phys.*, 280:306–344, 2015.
- [35] Mario Ricchiuto. *Contributions to the development of residual discretizations for hyperbolic conservation laws with application to shallow water flows*. Habilitation à diriger des recherches, Université Sciences et Technologies - Bordeaux I, December 2011.
- [36] Sergey Tkachenko, Sergey Gavriluk, and Jacques Massoni. Extended Lagrangian approach for the numerical study of multidimensional dispersive waves: Applications to the Serre-Green-Naghdi equations. *J.Comput.Phys.*, 477:111901, 2023.
- [37] Davide Torlo and Mario Ricchiuto. Model order reduction strategies for weakly dispersive waves. *Mathematics and Computers in Simulation*, 205:997–1028, 2023.
- [38] A. Treske. Undular bores (Favre-waves) in open channels - Experimental studies. *Journal of Hydraulic Research*, 32(3):355–370, May 1994.
- [39] Damien Violeau. Serre equations in channels and rivers of arbitrary cross section. *Journal of Hydraulic Engineering*, 149(7), 2023. Publisher: American Society of Civil Engineers.
- [40] Ge Wei, James T Kirby, Stephan T Grilli, and Ravishankar Subramanya. A fully nonlinear boussinesq model for surface waves. part 1. highly nonlinear unsteady waves. *Journal of Fluid Mechanics*, 294:71–92, 1995.
- [41] Patricio Winckler and Philip L.-F. Liu. Long waves in a straight channel with non-uniform cross-section. *Journal of Fluid Mechanics*, 770:156–188, May 2015.